J. metamorphic Geol., 2009, **27,** 19–40 doi:10.1111/j.1525-1314.2008.00800.x

Fifty-five-million-year history of oceanic subduction and exhumation at the northern edge of the Caribbean plate (Sierra del Convento mélange, Cuba)

C. LÁZARO,[1] A. GARCÍA-CASCO,[1,2] Y. ROJAS AGRAMONTE,[3] A. KRÖNER,[3] F. NEUBAUER[4] AND M. ITURRALDE-VINENT[5]

[1]*Departamento de Mineralogía y Petrología, Universidad de Granada, Avda Fuentenueva s/n, 18002 Granada, Spain (clazaro@ugr.es)*

[2]*Instituto Andaluz de Ciencias de la Tierra, CSIC-Universidad de Granada, Avda Fuentenueva s/n, 18002 Granada, Spain*

[3]*Institut für Geowissenschaften, Universität Mainz, 55099 Mainz, Germany*

[4]*Fachbereich Geographie, Geologie und Mineralogie, Universität Salzburg, Hellbrunner Strasse 34, A-5020 Salzburg, Austria*

[5]*Museo Nacional de Historia Natural, Obispo no. 61, Plaza de Armas, La Habana 10100, Cuba*

ABSTRACT Petrological and geochronological data of six representative samples of exotic blocks of amphibolite and associated tonalite-trondhjemite from the serpentinitic mélange of the Sierra del Convento (eastern Cuba) indicate counterclockwise *P–T* paths typical of material subducted in hot and young subduction zones. Peak conditions attained were ~750 °C and 15 kbar, consistent with the generation of tonalitic partial melts observed in amphibolite. A tonalite boulder provides a U-Pb zircon crystallization age of 112.8 ± 1.1 Ma, and Ar/Ar amphibole dating yielded two groups of cooling ages of 106–97 Ma (interpreted as cooling of metamorphic/magmatic pargasite) and 87–83 Ma (interpreted as growth/cooling of retrograde overprints). These geochronological data, in combination with other published data, allow the following history of subduction and exhumation to be established in the region: (i) a stage of hot subduction 120–115 Ma, developed upon onset of subduction; (ii) relatively fast near-isobaric cooling (25 °C Myr^{-1}) 115–107 Ma, after accretion of the blocks to the upper plate lithospheric mantle; (iii) slow syn-subduction cooling (4 °C Myr^{-1}) and exhumation (0.7 km Myr^{-1}) in the subduction channel 107–70 Ma; and (iv) fast syn-collision cooling (74 °C Myr^{-1}) and exhumation (5 km Myr^{-1}) 70–60 Ma.

Key words: Ar/Ar dating; Caribbean subduction; cooling/exhumation rates; *P–T–t* paths; SHRIMP dating.

INTRODUCTION

The dynamics of subduction zones and the speed at which rocks accreted to an overriding plate and/or incorporated into a subduction channel return to the surface are controversial topics. Studies of heating/cooling and burial/exhumation rates of high-pressure rocks provide firsthand insights into deep-seated processes and the mechanism of subduction and return, the results of which can be incorporated into plate tectonic models. Numerous studies have shown that a continuum exists between two distinct end-member types of exhumation of subducted rock complexes. Fast exhumation rates corresponding to rates of plate motion (> 1–10 km Myr^{-1}) have been determined for example in the Alps (Duchêne *et al.*, 1997; Rubatto & Hermann, 2001), the Aegean (Ring & Reischmann, 2002) and Papua New Guinea (Baldwin *et al.*, 2004). However, slow exhumation rates of < 0.1–1 km Myr^{-1} have been reported from the Franciscan complex of California (Anczkiewicz *et al.*, 2004; Tsujimori *et al.*, 2006), the Washington Cascade Range (Reiners *et al.*, 2002), the Sanbagawa belt in Japan (Wallis *et al.*, 2004) and the Caribbean (Krebs *et al.*, 2008). Cases of fast exhumation are generally related to the collision of thick and/or buoyant oceanic or continental lithosphere with the trench-fore arc–arc system, which is normally associated with the end of subduction. Cases of slow exhumation, on the other hand, appear to be typical of near-steady-state subduction. In this scenario, fragments of the subducted slab are incorporated into the overlying subduction channel, where the blocks are generally slowly exhumed (Gerya *et al.*, 2002). This is in contrast to fast exhumation where discrete tectonic events of collision and subsequent extension/collapse cause deep-seated rocks to rapidly ascend to the surface.

Observations on natural rocks have also established a variety of *P–T* paths for subducted material (Ernst, 1988), in agreement with geophysical calculations and modelling (Gerya *et al.*, 2002). Thus oceanic rocks exhumed in syn-subduction scenarios normally show

cold exhumation paths (clockwise cooling during decompression or counterclockwise cooling at depth). Whereas the corner flow model provides an explanation for the existence of counterclockwise *P–T* paths (Cloos, 1982), it appears that this type of path is not as general as the clockwise type. Counterclockwise *P–T* paths are considered to be characteristic of rocks subducted in juvenile subduction scenarios and, consequently, to document a transient thermal state during onset of subduction (e.g., Perchuk *et al.*, 1999; Gerya *et al.*, 2002; Wakabayashi, 2004; Willner *et al.*, 2004; Krebs *et al.*, 2008; García-Casco *et al.*, 2008a).

Here *P–T–t* data are presented for exotic blocks of epidote ± garnet amphibolite and associated trondhjemite from the Sierra del Convento mélange (eastern Cuba). Petrological and geochemical studies of the samples indicate that the blocks represent the partial melting products and residues of a mafic oceanic crust that was subducted during the earliest stage of subduction in the region (García-Casco *et al.*, 2008a; Lázaro & García-Casco, 2008). These fragments of oceanic crust were then accreted to the overriding plate and subsequently incorporated into the subduction channel, where they resided for tens of million years until they were finally exhumed in the latest Cretaceous, when collision started in the region (García-Casco *et al.*, 2006, 2008b). Previous petrological studies by García-Casco *et al.* (2006, 2008a) indicate that the blocks followed counterclockwise *P–T* paths during syn-subduction exhumation within a subduction channel. Building on this previous study, here we deal with the thermochronological aspects in an effort to determine heating/cooling and burial/exhumation rates from birth to demise of the associated subduction zone, and to constrain the geodynamic evolution of the Caribbean plate. To this end, SHRIMP zircon and Ar/Ar amphibole ages were determined in two samples studied by García-Casco *et al.* (2008a), for which detailed textural, mineralogical and *P–T* information is available, and in four samples specifically selected for the purpose of this study (see below). In addition, we give new detailed textural, mineral and *P–T* information for these new samples.

GEOLOGICAL SETTING

The Caribbean orogenic belt fringes the Caribbean plate, from Guatemala through the Antilles and northern South America. In the Greater Antilles, the belt documents the collision of a Mesozoic–Tertiary volcanic arc with buoyant parts of the North American plate during the Late Mesozoic and Tertiary (Fig. 1). In this northern branch of the margin of the Caribbean plate, the orogenic belt is mainly composed of oceanic material, including ophiolites and intra-oceanic volcanic arcs, as well as fragments of the southern borderlands of North America (Bahamas platform) and the Maya (Yucatan) block. All these terranes are well exposed in Cuba (Fig. 2a). The oceanic material includes the northern and eastern ophiolite belts and the Cretaceous and Palaeogene volcanic arcs (Iturralde-Vinent, 1998 and references therein). In the Cretaceous volcanic arc, the magmatic activity began in the Early Cretaceous (Aptian–Albian) and lasted until the Mid- to Late Campanian with a short interruption within the Santonian–Lower Campanian (Iturralde-Vinent, 1998). Serpentinite mélanges, associated with the ophiolite bodies all along the island, document subduction during the Cretaceous (120–70 Ma; García-Casco *et al.*, 2006 and references therein). The cessation of volcanic arc activity coincides with Late Cretaceous isotopic ages of metamorphosed continental terranes (mostly interpreted as cooling ages; Iturralde-Vinent *et al.*, 1996; García-Casco *et al.*, 2001; Stanek *et al.*, 2006), suggesting a stage of arc–continent collision during the Late Cretaceous (García-Casco *et al.*, 2008b).

In eastern Cuba, between the Nipe-Guacanayabo and Oriente faults, the ophiolitic belt comprises two large massifs: the Mayarí and Moa-Baracoa (Fig. 2a). These massifs have recently been referred to as 'eastern ophiolites' by Iturralde-Vinent *et al.* (2006) to emphasize their special geological character when compared

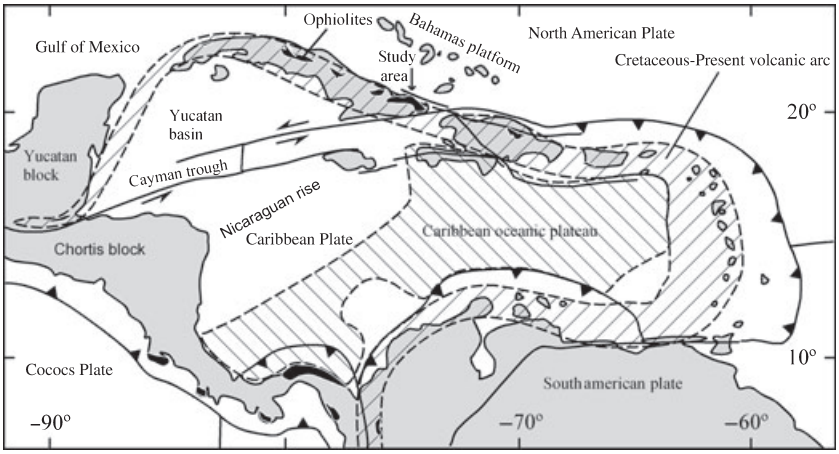

Fig. 1. Plate tectonic configuration of the Caribbean region, with important geological features including ophiolitic bodies and Cretaceous–Tertiary volcanic arc (compiled by García-Casco et al., 2006).

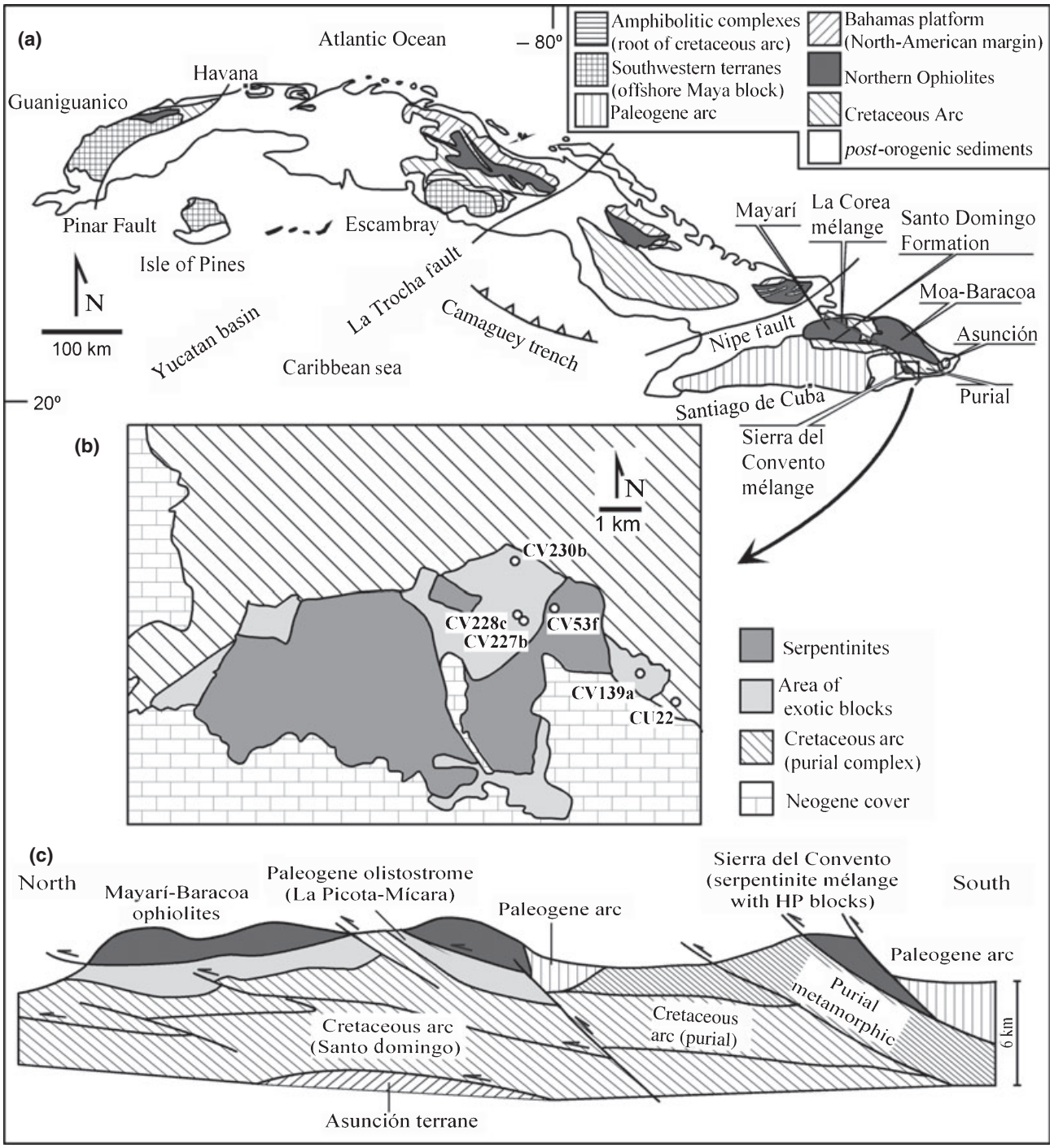

Fig. 2. (a) General geological map of Cuba (after Iturralde-Vinent, 1998) showing main geological units. (b) Geological map of the Sierra del Convento (after Kulachkov & Leyva, 1990) with location of sample sites. (c) Schematic cross-section of eastern Cuba (after Iturralde-Vinent, 1998).

with those of west-central Cuba. Element and isotopic geochemistry indicates a supra-subduction environment for the eastern ophiolites (Marchesi *et al.*, 2006; Proenza *et al.*, 2006). The Cretaceous volcanic arc formations have distinct geochemical signatures including tholeiitic, boninitic and calcalkaline (Proenza *et al.*, 2006). The volcanic arc Purial complex, located to the south of the ophiolitic massifs, has major and trace element geochemistry indicative of island arc tholeiitic and calcalkaline characteristics, and has been classically considered as the eastern continuation of the western and central Cuban Cretaceous arc (Fig. 2a;

Iturralde-Vinent *et al.*, 1996, 2006). The complex is strongly deformed and metamorphosed in the greenschist and blueschist facies (Boiteau *et al.*, 1972; Somin & Millán, 1981; Cobiella *et al.*, 1984; Millán, 1996) and appears to be the only occurrence of a subducted volcanic arc complex in Cuba. Regionally, the ophiolitic bodies in eastern Cuba lie structurally above the Purial Cretaceous volcanic arc complex, as opposed to central and western Cuba where the ophiolites tectonically underlie the Cretaceous volcanic arc suite. The Maastrichtrian–Danian Mícara and La Picota formations are composed of fragments and blocks from the ophiolitic bodies and the Cretaceous volcanic arc formations (Iturralde-Vinent, 1976, 1977; Cobiella *et al.*, 1984) and constitute syn-orogenic deposits reflecting the final obduction of the ophiolitic massifs in eastern Cuba onto the Cretaceous volcanic arc (Iturralde-Vinent *et al.*, 2006).

Serpentinite mélanges containing medium- to high-pressure metamorphic blocks occur at the base of the ophiolitic units in Cuba. In eastern Cuba, the most significant complexes are the Sierra del Convento and La Corea mélanges, both sharing similar lithological assemblages (Millán, 1996). The La Corea mélange is located in the Sierra de Cristal, associated with the Mayarí ophiolitic body (Fig. 2a) and overrides the volcanic arc Santo Domingo Formation, considered as the non-metamorphosed counterpart of the Purial complex (Iturralde-Vinent *et al.*, 2006). The Sierra del Convento mélange, located southward, overrides the Purial complex (Fig. 2b,c). These mélanges have been interpreted as fragments of the subduction channel associated with south-westward-directed subduction on the leading edge of the Caribbean plate during the Cretaceous (García-Casco *et al.*, 2006, 2008a,b).

THE SIERRA DEL CONVENTO MÉLANGE

Metamorphic blocks from the Sierra del Convento mélange are variable in composition. The described lithologies include amphibolite, blueschist, greenschist, quartzite, impure quartz-feldspathic rocks, metagreywacke and metapelite, whereas eclogite is rare or absent (Somin & Millán, 1981; Kulachkov & Leyva, 1990; Hernández & Canedo, 1995; Leyva, 1996; Millán, 1996; García-Casco *et al.*, 2008a). However, the dominant rock type is a MORB-derived high-temperature epidote ± garnet amphibolite. The amphibolites commonly contain centimetre- to metre-size layers, pockets and veins of leucocratic material of trondhjemitic to tonalitic composition (henceforth termed 'trondhjemites'), locally with pegmatoid texture. García-Casco *et al.* (2008a) demonstrated that the trondhjemitic segregations formed upon fluid-assisted partial melting of the amphibolites at ~750 °C and 14–16 kbar. Major and trace element and isotopic data also support this view (Lázaro & García-Casco, 2008). The process took place during subduction of the oceanic crust in a hot-subduction scenario and, importantly, subsequent exhumation occurred in a syn-subduction setting, allowing the blocks in the mélange to follow counterclockwise *P–T* paths (García-Casco *et al.*, 2006, 2008a; García-Casco, 2007). These authors also showed that the high-grade blocks of amphibolite and associated trondhjemite represent the first subducted material and their partial melts. Thus, these blocks should have been accreted to the overriding plate soon after initiation of subduction, and their *P–T–t* evolution, addressed in this study, may shed light on the early history of the subduction of the region.

Published geochronological data for the Sierra del Convento mélange are scarce and imprecise, precluding the development of a precise metamorphic and geodynamic model for the history of subduction in the region. Available K-Ar mineral ages of metamorphic blocks from the Sierra del Convento range from 116 to 82 Ma (Somin & Millán, 1981; Hatten *et al.*, 1989; Somin *et al.*, 1992; Iturralde-Vinent *et al.*, 1996). U-Pb zircon ages of 126–120 Ma and 105–103 Ma have been interpreted as magmatic ages of the subducting crust and its metamorphism, respectively (Hatten *et al.*, 1989). A similar wide range of K-Ar ages (125–66 Ma) is available for metamorphic blocks from the La Corea mélange (Adamovich & Chejovich, 1964; and references above). Metamorphism in the underlying volcanic arc Purial complex occurred in the latest Cretaceous. Somin *et al.* (1992) provided a K-Ar whole-rock age of 75 ± 5 Ma for a low-grade schist from this complex, and Iturralde-Vinent *et al.* (2006) suggested 75–72 Ma as the timing of metamorphism based on stratigraphic–palaeontological arguments. A Maastrichtian–Danian (68–63 Ma) depositional age for the syn-orogenic Mícara and La Picota formations (Iturralde-Vinent *et al.*, 2006) establishes an upper limit for regional metamorphism in the region. In short, all these data suggest subduction from the late Early Cretaceous until the Late Cretaceous, whereas the Purial complex appears to have impinged upon the subduction zone in the Late Cretaceous, when collision began in the region. By Maastrichtian time, the ophiolites, mélanges and Cretaceous volcanic arc complexes of eastern Cuba were already being exhumed and close to the Earth's surface. In this study, $^{40}Ar/^{39}Ar$ dating of amphibole from amphibolites and trondhjemites and SHRIMP analysis of zircon from a tonalitic rock have been performed to clarify the history of oceanic subduction and associated exhumation.

ANALYTICAL TECHNIQUES

Mineral compositions were obtained by wavelength-dispersive spectrometry (WDS) with a Cameca SX-50 microprobe (University of Granada), operated at 20 kV and 20 nA, and synthetic SiO_2, Al_2O_3, $MnTiO_3$, Fe_2O_3, MgO and natural diopside, albite and sanidine as calibration standards, and by energy-dispersive spectrometry (EDS) with a Zeiss DSM 80 950 scanning

microscope, equipped with a Link Isis series 300 Analytical Pentafet system, operated at 20 kV and 1–2 nA beam current, with counting times of 50–100 s, and the same calibration standards as above. Amphibole compositions were normalized to 23 oxygen and Fe^{3+} was estimated according to the scheme of Leake *et al.* (1997). Garnet was normalized to 8 cations and 12 oxygen and Fe^{3+} was estimated by stoichiometry. Epidote, feldspar, lawsonite and kyanite were normalized to 12.5, 8, 8 and 5 oxygen, respectively, and $Fe_{total} = Fe^{3+}$. Mica, chlorite and pumpellyite were normalized to 22, 28 and 24.5 oxygen, respectively, and $Fe_{total} = Fe^{2+}$. Mineral and end-member abbreviations are after Kretz (1983) except for amphibole (Amp). The atomic concentration of elements per formula units is abbreviated 'apfu'. Representative chemical analyses are given in Table 1 (see García-Casco *et al.*, 2006, 2008a, for mineral chemistry of samples CV230b & CV228c).

Elemental XR images were obtained with the same CAMECA SX-50 microprobe operated at 20 kV, ranging from 250 to 300 nA beam current, with step (pixel) size ranging from 7 to 9 μm and counting time ranging from 25 to 100 ms. The images were processed using the software IMAGER (R.L. Torres-Roldán & A. García-Casco, unpublished software). These data consist of the XR signals of Kα lines of the elements or element ratios indicated (colour-coded; expressed in counts $nA^{-1}\ s^{-1}$) corrected for 3.5-μs deadtime and with voids, polish defects, and all other mineral phases masked out, overlain onto a grey scale base-layer calculated with the expression $\sum[(\text{counts } nA^{-1}s^{-1})_i(A_i)]$ (A = atomic number, i = Si, Ti, Al, Fe, Mn, Mg, Mg, Ca, Na and K) that contains the basic textural information of the scanned areas.

Cathodoluminescence (CL) images of the dated zircon (sample CU22) were obtained prior to SHRIMP analysis, to distinguish between different zircon domains. CL imaging was undertaken in the Centre for Microscopy and Microanalysis at the University of Western Australia, Perth, on a JEOL 6400 scanning electron microscope, operated at 15 kV accelerating voltage and 5 nA beam current. The U–Pb ion microprobe data were obtained on the SHRIMP II (B) of the John de Laeter Centre of Mass Spectrometry at Curtin University, Australia (De Laeter & Kennedy, 1998). Clear euhedral zircon approximately 80–150 μm in length from sample CU22 was handpicked and mounted in epoxy resin together with other samples and chips of the Perth zircon standard CZ3. Details on the SHRIMP procedure, age calculation and error assessment can be found in Compston *et al.* (1992), Stern (1997), Nelson (1997) and Williams (1998).

Precise dating of young zircon by ion-microprobe is best achieved by using $^{206}Pb/^{238}U$ ages (see Black *et al.*, 2003; for explanation), and the reduced $^{206}Pb/^{238}U$ ratios were normalized to Perth standard CZ3 ($^{206}Pb/^{238}U = 0.09432$, age: 564 Ma). Sensitivity was about 26 cps $ppm^{-1}\ nA^{-1}$ Pb on CZ3. Analyses of samples and standards were alternated to allow assessment of Pb^+/U^+ discrimination. Raw data reduction followed the method of Nelson (1997). Common-Pb corrections were applied using the ^{204}Pb-correction method. The zircon of CU22 had very low counts on ^{204}Pb, and in these cases it was assumed that common lead is surface-related (Kinny, 1986) and the isotopic composition of Broken Hill lead was used for correction. The analytical data are presented in Table 2. Errors on individual analyses are given at the 1-sigma level and are based on counting statistics and include the uncertainty in the standard U/Pb age (Nelson, 1997). The error for pooled analyses is at the 2-sigma or 95% confidence interval. The analyses are presented in Table 2.

Preparation of mineral samples before and after irradiation for $^{40}Ar/^{39}Ar$ analyses was carried out at the ARGONAUT Laboratory in the Institute of General Geology and Geodynamics at the University of Salzburg (Austria). Hornblende concentrates were prepared by crushing, sieving, flotation and handpicking of grains in the size ranges 250–200 and 250–125 μm. For isotopic measurements, 10–20 grains per sample were selected, and the mineral concentrates were packed in aluminium foil and loaded in quartz vials. For calculation of the J-values, flux monitors were placed between each four and five unknown samples, which yielded a distance of ~5 mm between adjacent flux monitors. The sealed quartz vials were irradiated in the MTA KFKI reactor (Debrecen, Hungary) for 16 h. Correction factors for interfering isotopes were calculated from 10 analyses of two Ca-glass samples and 22 analyses of two pure K-glass samples, and are: $^{36}Ar/^{37}Ar_{(Ca)} = 0.00026025$, $^{39}Ar/^{37}Ar_{(Ca)} = 0.00065014$ and $^{40}Ar/^{39}Ar_{(K)} = 0.015466$. Variations in the flux of neutrons were monitored with a DRA1 sanidine standard for which a $^{40}Ar/^{39}Ar$ plateau age of 25.03 ± 0.05 Ma has been reported by Wijbrans *et al.* (1995). After irradiation, the minerals were unpacked from the quartz vials and aluminium-foil packets and handpicked into 1-mm-diameter holes within one-way Al-sample holders.

$^{40}Ar/^{39}Ar$ analyses were carried out using a UHV Ar-extraction line equipped with a combined MERCHANTEK™ UV/IR laser ablation facility and a VG-ISOTECH™ NG3600 Mass Spectrometer and follow methods described in Handler *et al.* (2004). Stepwise heating analyses of samples were performed using a defocused (~1.5 mm diameter) 25 W CO_2-IR laser operating in Tem00 mode at wavelengths between 10.57 and 10.63 μm. The laser is controlled from a PC, and the position of the laser within the sample is monitored through a double-vacuum window on the sample chamber via a video camera in the optical axis of the laser beam on the computer screen. Gas clean-up was performed using one hot and one cold Zr-Al SAES getter. Gas admittance and pumping of the mass spectrometer and the Ar-extraction line are computer-controlled

Table 1. Representative analyses of calcic and sodic (Gl) amphiboles (normalized to 22 O and 2 OH), garnet (normalized to 12 O), and epidote (normalized to 12 O and 1 OH).

Phase	Calcic amphibole					Gl	Garnet	Epidote							
Type of rock	Amphibolite		Trondhjemite			Amphibolite	Amphibolite	Amphibolite	Trondhjemite						Amphibolite
Sample	CV139a		CV227b		CV53f	CV139a	CV139a	CV139a	CV227b		CV53f		CU22		CV139a
Type	Peak	Retro	Peak	Retro	Peak	Retro	Peak	Peak	Peak	Retro	Peak	Retro	Peak	Retro	Retro
SiO_2	43.07	55.08	44.04	55.32	41.97	56.73	38.07	38.89	39.01	39.54	38.88	38.51	38.62	39.65	66.86
TiO_2	1.1	0.03	0.6	0.08	0.78	0.02	0.07	0.05	0.16	0.07	0.11	0.26	0.05	0.05	
Al_2O_3	14.09	1.13	16.39	4.31	17.09	11.58	21.95	31.69	28.58	32.84	26.5	33.03	26.94	30.44	19.83
FeO_{total}	12	12.38	9.12	3.89	8.55	12.09	22.07	2.63	6.73	1.05	8.54	0.58	8.66	3.99	0.41
MnO	0.07	0.08	0.13	0.09	0.11	0.07	0.35	0.05	0.13	0	0.06	0.04	0.1	0.04	0.01
MgO	12.33	16.22	13.09	20.94	13.51	8.67	4.65	0.02	0.16	0.02	0.26	0.12	0.02	0.28	
CaO	11.35	12.01	10.19	11.89	11.05	0.8	12.8	23.79	22.91	23.99	22.85	24.83	22.32	22.93	0.39
BaO					0.02							0	0.01	0	
Na_2O	2.61	0.52	3.41	1.09	3.28	7.02									11.74
K_2O	0.62	0.05	0.29	0.07	0.14	0.03									0.16
H_2O[a]	2.04	2.09	2.09	2.18	2.07	2.15		1.95	1.94	1.97	1.92	1.96	1.92	1.96	
Total	99.29	99.6	99.37	99.86	98.57	99.15	99.95	99.06	99.63	99.46	99.13	99.32	98.63	99.33	99.4
Si	6.32	7.89	6.32	7.6	6.09	7.9	2.95	2.99	3.01	3.01	3.03	2.95	3.02	3.04	2.95
Ti	0.12	0	0.07	0.01	0.09	0	0	0	0.01	0	0.01	0.01	0	0	
Al	2.43	0.19	2.77	0.7	2.92	1.9	2	2.87	2.6	2.95	2.43	2.98	2.48	2.75	1.03
Fe^{3+}	0.17	0.09	0.21	0.18	0.22	0.09	0.1	0.17	0.43	0.07	0.56	0.04	0.57	0.26	0.02
Fe^{2+}	1.3	1.39	0.88	0.27	0.81	1.32	1.33								
Mn	0.01	0.01	0.02	0.01	0.01	0.01	0.02	0	0.01	0	0	0	0.01	0	0
Mg	2.7	3.47	2.8	4.29	2.92	1.8	0.54	0	0.02	0	0.03	0.01	0	0.03	
Ca	1.78	1.84	1.57	1.75	1.72	0.12	1.06	1.96	1.89	1.96	1.91	2.04	1.87	1.88	0.02
Ba					0							0	0	0	
Na	0.74	0.14	0.95	0.29	0.92	1.9									1
K	0.12	0.01	0.05	0.01	0.03	0									0.01
Mg#	0.67	0.71	0.76	0.94	0.78	0.58	0.29								

Phase	Plagioclase					Paragonite				Phengite				Chlorite				Kyanite
Type of rock	Trondhjemite					Trondhjemite				Amphibolite		Trondhjemite		Amphibolite	Trondhjemite			Trondhjemite
Sample	CV227b		CV53f		CU22	CV227b		CV53f		CV139a		CV53f	CU22	CV139a	CV227b	CV53f	CU22	CV53f
Type	Peak	Retro	Peak	Retro	Retro	Peak	Retro	Peak	Retro	Peak	Retro	Retro	Retro	Retro	Retro	Retro	Retro	Peak
SiO_2	65.53	67.82	63.27	68.27	67.32	46.35	46.69	45.88	45.8	47.24	50.15	51.27	52.28	25.68	30.38	29.18	26.01	36.06
TiO_2						0.22	0.07	0.34	0.23	0.75	0.18	0.23	0.05					0.01
Al_2O_3	21.42	19.45	22.85	19.62	19.5	39.89	40.14	39.02	39.74	31.37	28.29	26.83	24.48	19.3	19.41	19.78	19.68	62.48
FeO_{total}	0.09	0.1	0	0	0.13	0.42	0.19	0.54	0.49	1.7	2.1	1.43	3.37	29.76	12.13	13.77	25.89	0.6
MnO	0.01	0	0.01	0	0.01	0	0	0	0.03	0	0	0	0	0.57	0.05	0.1	0.24	0
MgO						0.2	0.13	0.26	0.17	2.31	3.23	4.17	3.62	12.31	25.45	24.59	15.48	
CaO	2.19	0.1	4.06	0.06	0.46	0.65	0.29	0.59	0.62	0	0	0.17	0.01					
BaO			0.02	0	0.04			0.37	0.02	1.67	1.16		0.44					
Na_2O	10.31	11.74	9.34	12.01	11.74	6.48	7.3	6.11	7.21	1.12	0.7	0.32	0.12					
K_2O	0.04	0.02	0.07	0.01	0.04	1.09	0.57	2.11	0.77	9.3	10.15	10.85	10.48					
H_2O[a]						4.68	4.7	4.64	4.66	4.46	4.49	4.5	4.45	11.07	12.27	12.13	11.3	
Total	99.59	99.23	99.62	99.97	99.26	99.98	100.07	99.84	99.73	99.91	100.45	99.76	99.42	98.68	99.7	99.55	98.68	99.14
Si	2.89	2.99	2.81	2.99	2.97	5.93	5.95	5.93	5.89	6.35	6.7	6.83	7.05	5.57	5.94	5.77	5.53	0.98
Ti						0.02	0.01	0.03	0.02	0.08	0.02	0.02	0.01	0	0	0		0
Al	1.11	1.01	1.19	1.01	1.01	6.02	6.03	5.95	6.02	4.97	4.45	4.21	3.89	4.93	4.47	4.61	4.93	2.01
Fe^{3+}	0	0	0	0	0													0.01
Fe^{2+}						0.05	0.02	0.06	0.05	0.19	0.23	0.16	0.38	5.39	1.98	2.28	4.6	
Mn	0	0	0	0	0	0	0	0	0	0	0	0	0	0.1	0.01	0.02	0.04	0
Mg						0.04	0.02	0.05	0.03	0.46	0.64	0.83	0.73	3.98	7.42	7.25	4.9	
Ca	0.1	0	0.19	0	0.02	0.09	0.04	0.08	0.09	0	0	0.02	0					
Ba			0	0	0			0.02	0	0.09	0.06		0.02					
Na	0.88	1	0.8	1.02	1.01	1.61	1.81	1.53	1.8	0.29	0.18	0.08	0.03					
K	0	0	0	0	0	0.18	0.09	0.35	0.13	1.6	1.73	1.84	1.8					
Mg#						0.45	0.55	0.46	0.38	0.71	0.73	0.84	0.66	0.42	0.79	0.76	0.52	

[a]Calculated by stoichiometry.
Blanks indicate elements not analysed.

using pneumatic valves. The NG3600 is an 18-cm-radius 60° extended geometry instrument, equipped with a bright Nier-type source operated at 4.5 kV.

Measurements were performed on an axial electron multiplier in static mode on a single-collector instrument. Peak-jumping and stability of the magnet are controlled by a Hall probe. For each increment, the intensities of ^{36}Ar, ^{37}Ar, ^{38}Ar, ^{39}Ar and ^{40}Ar were measured, and the baseline readings on mass 35.5 are automatically subtracted. Intensities of the peaks were

Table 2. SHRIMP II analytical data for spot analyses of single zircons from sample CU22 and ages.

Sample no.	U (ppm)	Th (ppm)	$^{206}Pb/^{204}Pb$	$^{208}Pb/^{206}Pb$	$^{207}Pb/^{206}Pb$	$^{206}Pb/^{238}U$	$^{207}Pb/^{235}U$	Age (Ma) ± error × 10^{-6}
Cu 22-1-1	74	12	14587	0.0538 ± 0.2230	0.0494 ± 0.1012	0.0175 ± 0.0114	0.119 ± 0.010	112 ± 2
Cu 22-2-1	136	62	5122	0.1348 ± 0.1291	0.0464 ± 0.1509	0.0177 ± 0.0113	0.113 ± 0.015	113 ± 2
Cu 22-3-1	184	99	6248	0.1677 ± 0.1550	0.0467 ± 0.0214	0.0174 ± 0.0172	0.112 ± 0.022	111 ± 2
Cu 22-3-2	127	51	3792	0.1156 ± 0.1298	0.0450 ± 0.1333	0.0177 ± 0.0113	0.110 ± 0.014	113 ± 3
Cu 22-4-1	139	64	5224	0.1459 ± 0.1062	0.0489 ± 0.1268	0.0175 ± 0.0114	0.118 ± 0.013	112 ± 3
Cu 22-5-1	83	30	8718	0.1167 ± 0.1534	0.0453 ± 0.1589	0.0177 ± 0.0169	0.111 ± 0.016	113 ± 2
Cu 22-6-1	101	34	21988	0.1106 ± 0.0515	0.0492 ± 0.0467	0.0178 ± 0.0112	0.120 ± 0.005	114 ± 1
Cu 22-7-1	68	20	1637	0.0835 ± 1.0347	0.0464 ± 0.0754	0.0176 ± 0.0398	0.112 ± 0.077	112 ± 4
Cu 22-8-1	72	24	49791	0.1102 ± 0.0544	0.0487 ± 0.0472	0.0177 ± 0.0113	0.119 ± 0.005	113 ± 1

Note: Errors of ratios and ages are at the 1-sigma level.

back-extrapolated over 16 measured intensities to the time of gas admittance either by a straight line or a curved fit, depending on the shape of curve. Fit by a straight line is typical for low intensities and curved fit for high intensities. Intensities were corrected for system blanks, background, post-irradiation decay of ^{37}Ar and interfering isotopes. Isotopic ratios, ages and errors for individual steps were calculated following suggestions by McDougall & Harrison (1999) and using decay constants recommended by Steiger & Jäger (1977). Plateau and integrated ages were calculated using the ISOPLOT/EX 3.00 software (Ludwig, 2001). Time-scale calibration follows Gradstein & Ogg (2005). The analyses are presented in Table 3.

SAMPLE DESCRIPTION

Two representative epidote–garnet amphibolites (samples CV230b & CV139a) and four trondhjemite-tonalite rocks (samples CV227b, CV228c, CV53f & CU22) were selected for Ar/Ar and SHRIMP analysis (for location, see Fig. 2b). Mineral assemblages, textures, mineral chemistry and *P–T* calculations of these samples are provided below. Samples CV230b & CV228c were studied by García-Casco *et al.* (2008a). The reader is referred to this paper for figures, tables and *P–T* calculations documenting these samples. Bulk-rock geochemistry of all samples is provided by Lázaro & García-Casco (2008).

The sample used for SHRIMP dating (CU22) was recovered from a boulder of tonalitic composition collected in the bed of the Yacabo River. Mineral assemblages, textures and mineral compositions (see below) indicate that CU22 is an eroded fragment from the mélange. The use of a boulder rather than in-situ samples is justified because CU22 is the only sample out of several that have yielded zircon (in spite of having processed several kilograms per sample collected). The lack of zircon in blocks of the mélange is not surprising in view of their low Zr concentration (Lázaro & García-Casco, 2008). This feature is a consequence of the MORB chemistry of the amphibolite protoliths and the compatible behaviour of Zr during partial melting of amphibolites (Lázaro & García-Casco, 2008).

In all samples, calcic amphibole shows a heterogeneous composition with peak Ti-rich pargasite compositions overprinted by Ti-poor edenite-magnesiohornblende-actinolite compositions that also constitute separate grains in the matrix formed throughout the retrograde path (Fig. 3b,d, and see below). These compositions translate into the brown and green colours of amphibole seen under the petrographic microscope. Brownish and greenish amphiboles were carefully separated for dating in amphibolite sample CV139a in an effort to test the chemical composition effects of amphibole on the Ar/Ar systematics and to better constrain the timing of amphibole growth during retrogression. In all samples, the grain-size fractions of Ar/Ar-dated amphibole grains were 250–125 μm, except in CV53f (250–200 μm).

Petrography

Amphibolites

Sample CV230b contains a peak metamorphic assemblage consisting of pargasitic amphibole, epidote, garnet, titanite, rutile and apatite. Pargasitic amphibole comprises most of the matrix and is oriented parallel to a weak foliation (Fig. 3a,b). Garnet forms large porphyroblasts (up to 1.5 cm in diameter) that include pargasitic amphibole, epidote, rutile and titanite. Retrograde overprints are faint and consist of edenite-magnesiohornblende-actinolite, glaucophane, albite, chlorite and pumpellyite. The rims of pargasitic amphibole are replaced by actinolite, glaucophane, chlorite and albite. Garnet is slightly replaced at the rims and along fractures by edenite-magnesiohornblende-actinolite, chlorite, pumpellyite and albite.

Sample CV139a is weakly foliated and comprises a peak metamorphic assemblage consisting of pargasitic amphibole, epidote, garnet, rutile, titanite, quartz and phengite. Pargasitic amphibole includes epidote and titanite. Garnet porphyroblasts show inclusions of amphibole and titanite. Blocky epidote appears in the matrix and is intergrown with quartz. Faintly oriented phengite is distributed in the matrix. The retrograde overprints consist of edenite-magnesiohornblende-actinolite, glaucophane, phengite, quartz, chlorite,

Table 3. $^{40}Ar/^{39}Ar$ analytical results.

Step	$^{36}Ar/^{39}Ar$[a]	$^{37}Ar/^{39}Ar$[b]	$^{40}Ar/^{39}Ar$[a]	$\%^{40}Ar$[c]	$\%^{39}Ar$	Age (Ma)
Sample CV139a, brownish amphibole (125–250 μm), J = 0.00612 ± 0.0000327						
1	0.54549 ± 0.00217	1.8900 ± 0.0018	161.387 ± 0.738	0.1	2.3	3.6 ± 8.1
2	0.43199 ± 0.00171	3.7334 ± 0.0028	130.456 ± 0.621	2.1	2.0	33.7 ± 6.7
3	0.35163 ± 0.00160	4.0826 ± 0.0022	107.653 ± 0.516	3.5	2.4	44.2 ± 5.6
4	0.07358 ± 0.00036	7.4136 ± 0.0014	29.983 ± 0.108	27.5	8.9	95.0 ± 1.2
5	0.08751 ± 0.00045	6.2030 ± 0.0014	33.619 ± 0.136	23.1	7.3	88.9 ± 1.5
6	0.11208 ± 0.00046	7.3311 ± 0.0021	40.634 ± 0.144	18.5	5.5	87.3 ± 1.6
7	0.03044 ± 0.00012	8.2478 ± 0.0009	17.359 ± 0.036	48.2	29.3	97.1 ± 0.6
8	0.00568 ± 0.00012	8.2313 ± 0.0002	10.217 ± 0.037	83.6	42.3	98.9 ± 0.6
Sample CV139a, greenish amphibole (125–250 μm), J = 0.006134 ± 0.0000321						
1	1.16555 ± 0.01241	2.0136 ± 0.0101	358.915 ± 4.871	4.0	1.0	155.3 ± 49.5
2	0.28847 ± 0.00193	14.6566 ± 0.0112	89.994 ± 0.643	5.3	3.4	64.3 ± 6.9
3	0.08181 ± 0.00047	13.9025 ± 0.0037	30.859 ± 0.143	21.7	14.0	84.4 ± 1.6
4	0.05377 ± 0.00026	9.3327 ± 0.0016	23.156 ± 0.078	31.4	24.6	86.6 ± 0.9
5	0.13565 ± 0.00110	9.1524 ± 0.0042	47.036 ± 0.338	14.8	5.3	83.1 ± 3.6
6	0.09469 ± 0.00078	10.8091 ± 0.0038	34.867 ± 0.237	19.7	8.0	83.8 ± 2.5
7	0.01196 ± 0.00021	1.2220 ± 0.0004	11.083 ± 0.062	68.1	43.6	82.5 ± 0.8
Sample CV230b, amphibole (125–250 μm), J = 0.006177 ± 0.0000306						
1	2.27100 ± 0.02458	14.3747 ± 0.0333	683.498 ± 10.041	1.8	0.6	145.9 ± 103.2
2	0.36406 ± 0.00261	13.4384 ± 0.0114	110.140 ± 0.866	2.3	2.0	39.8 ± 9.4
3	0.07772 ± 0.00057	11.9882 ± 0.0031	30.021 ± 0.172	23.5	8.1	87.3 ± 1.9
4	0.01966 ± 0.00012	10.2710 ± 0.0010	12.976 ± 0.035	55.2	40.3	86.9 ± 0.6
5	0.21883 ± 0.00203	11.6813 ± 0.0094	73.093 ± 0.650	11.5	2.0	101.7 ± 6.9
6	0.11783 ± 0.00127	11.2745 ± 0.0049.	43.129 ± 0.384	19.3	3.5	100.0 ± 4.1
7	0.02871 ± 0.00023	11.3065 ± 0.0017	16.852 ± 0.070	49.6	20.5	100.7 ± 0.9
8	0.01437 ± 0.00032	12.3936 ± 0.0005	11.212 ± 0.094	62.1	23.1	86.7 ± 1.1
Sample CV227b, amphibole (125–250 μm), J = 0.006192 ± 0.0000304						
1	1.64532 ± 0.02761	6.3305 ± 0.0242	563.922 ± 12.288	13.8	0.7	714.9 ± 92.4
2	0.92187 ± 0.01638	11.1445 ± 0.0382	319.737 ± 6.728	14.8	0.5	473.9 ± 57.8
3	0.28281 ± 0.00474	7.0329 ± 0.0111	99.209 ± 1.534	15.8	1.1	172.9 ± 15.6
4	0.03337 ± 0.00042	12.6501 ± 0.0035	17.895 ± 0.126	44.9	10.5	98.5 ± 1.4
5	0.02615 ± 0.00039	14.8121 ± 0.0043	14.173 ± 0.118	45.5	10.1	83.4 ± 1.3
6	0.02189 ± 0.00035	14.6433 ± 0.0036	13.218 ± 0.105	51.1	11.2	86.6 ± 1.2
7	0.03802 ± 0.00053	15.7151 ± 0.0056	20.015 ± 0.161	43.9	7.8	109.2 ± 1.8
8	0.02629 ± 0.00029	16.0111 ± 0.0032	14.747 ± 0.087	47.3	16.6	90.2 ± 1.0
9	0.01019 ± 0.00024	15.7268 ± 0.0004	10.717 ± 0.070	71.9	41.6	97.7 ± 0.9
Sample CV228c, amphibole (125–250 μm), J = 0.006221 ± 0.0000305						
1	1.24131 ± 0.02753	9.3940 ± 0.0440	481.765 ± 12.487	23.9	0.5	982.6 ± 81.4
2	0.33707 ± 0.00599	12.6461 ± 0.0255	129.488 ± 2.093	23.1	1.4	319.1 ± 19.7
3	0.15038 ± 0.00631	16.1081 ± 0.0404	53.843 ± 1.956	17.5	1.2	116.7 ± 20.6
4	0.01792 ± 0.00030	17.6270 ± 0.0042	11.843 ± 0.090	55.3	25.4	87.4 ± 1.0
5	0.02346 ± 0.00034	19.6069 ± 0.0039	13.573 ± 0.102	48.9	23.1	90.2 ± 1.2
6	0.11662 ± 0.00283	22.7785 ± 0.0214	40.195 ± 0.853	14.3	2.8	83.2 ± 9.2
7	0.03068 ± 0.00047	19.2998 ± 0.0062	14.537 ± 0.140	37.6	16.6	77.2 ± 1.5
8	0.01987 ± 0.00059	20.7465 ± 0.0009	13.841 ± 0.176	57.6	29.0	105.5 ± 1.9
Sample CV53f, amphibole (200–250 μm), J = 0.006333 ± 0.0000341						
1	9.07365 ± 1.21369	69.7959 ± 2.2906	2827.290 ± 519.703	5.2	0.1	1254.3 ± 2962.6
2	4.90865 ± 0.14901	3.4822 ± 0.0425	1550.171 ± 63.735	6.4	0.4	886.1 ± 445.6
3	7.28908 ± 0.16446	5.5300 ± 0.0374	2214.258 ± 69.368	2.7	0.6	589.0 ± 571.8
4	2.43602 ± 0.05798	10.1098 ± 0.0600	722.972 ± 23.692	0.4	0.5	44.2 ± 264.1
5	0.76276 ± 0.01411	10.3975 ± 0.0345	256.884 ± 5.308	12.3	1.1	337.6 ± 50.3
6	0.07911 ± 0.00157	27.2675 ± 0.0196	30.666 ± 0.473	23.8	6.9	105.8 ± 5.1
7	0.02959 ± 0.00023	27.6012 ± 0.0068	14.303 ± 0.070	38.9	42.8	87.1 ± 0.9
8	0.13545 ± 0.00193	25.9481 ± 0.0248	44.529 ± 0.596	10.1	5.5	73.8 ± 6.6
9	0.07505 ± 0.00100	29.3309 ± 0.0148	29.913 ± 0.302	25.9	11.7	112.6 ± 3.3
10	0.02602 ± 0.00073	32.7285 ± 0.0016	14.015 ± 0.217	45.1	30.6	100.2 ± 2.4

Note: Errors of ratios, J-values, and ages are at 1-sigma level.
[a]Measured.
[b]Corrected for postirradiation decay of ^{37}Ar.
[c]Non-atmospheric ^{40}Ar.

albite and pumpellyite. Pargasite is replaced by edenite-magnesiohornblende-actinolite and glaucophane. Garnet is slightly retrogressed and replaced by actinolite, glaucophane, phengite, chlorite, albite and pumpellyite at the rims and along fractures (Fig. 3c,d).

Trondhjemites

Samples CV227b & CV228c are very similar in chemical and mineralogical compositions and microfabrics. They are not foliated and have a primary (magmatic) mineral paragenesis composed of plagioclase, quartz, paragonite, epidote, pargasitic amphibole, rutile and titanite (Fig. 3e). Lawsonite (in sample CV228c), clinozoisite, albite, phengite and a second generation of fine-grained paragonite formed as retrograde alteration products of magmatic plagioclase and paragonite. Retrograde tremolite, chlorite and pumpellyite overprint pargasitic amphibole.

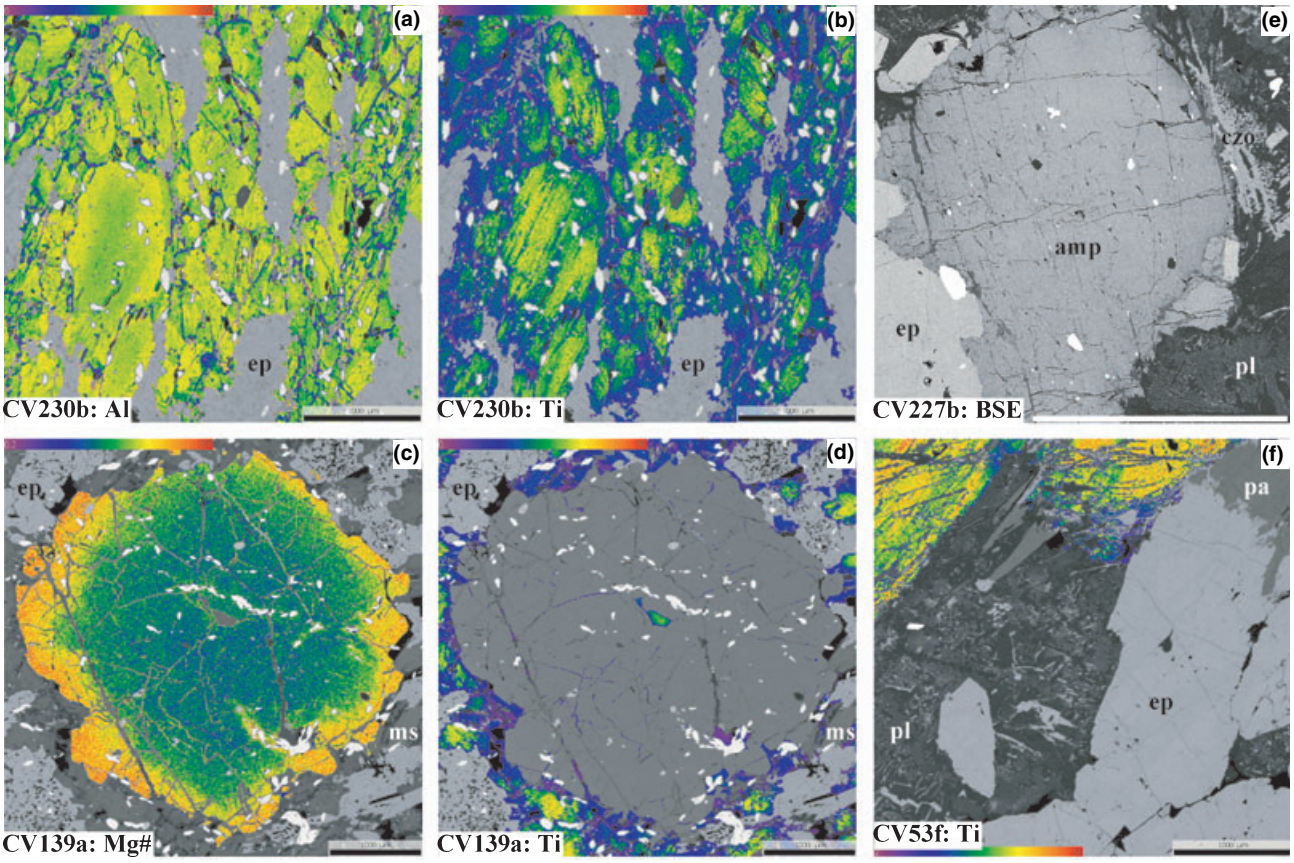

Fig. 3. XR and BSE images showing key textural and compositional data of studied minerals. (a) Al-Kα XR image of amphibolite sample CV230b showing heterogeneous composition of calcic amphibole. Note that retrograde grains/compositions (dark-green to purple) of edenite-magnesiohornblende-actinolite overprint matrix edenite (cores)-pargasite grains/compositions. (b) Ti-Kα XR image of the same amphiboles as in (a). The cores of primary Ti-richer compositions (green) and the Ti-poorer rims and fine-grained overprints (blue-purple) stand out clearly. (c) Mg-Kα/(Mg-Kα + Fe-Kα) XR image of garnet from amphibolite CV139a showing prograde growth zoning. (d) Ti-Kα XR image of calcic amphibole in the same area as in (c). The cores of primary Ti-richer compositions of matrix grains and inclusions (green) are overgrown/re-equilibrated by Ti-poorer (blue-purple) compositions located preferentially close to garnet rims and along fractures. (e) BSE image of magmatic amphibole, epidote and plagioclase from trondhjemite sample CV227b. Retrograde clinozoisite overprints plagioclase. (f) Ti-Kα XR image of calcic amphibole from sample CV53f showing overprints along fractures and rims by Ti-poorer magnesiohornblende-tremolite. Also shown are magmatic epidote, plagioclase and paragonite, and the retrograde overprints (mostly clinozoisite and paragonite) in plagioclase. Scale bar: 1 mm. Colour scale bar in the XR images (counts/nA/s) indicates high (red) and low (purple) concentrations.

Sample CV53f is a somewhat coarse-grained trondhjemitic rock with a magmatic mineral association composed of plagioclase, epidote, pargasitic amphibole, paragonite (all of which may reach centimetre grain size) and rutile (Fig. 3f). Relict crystals of kyanite (likely magmatic) are present as inclusions within magmatic epidote. Fine-grained paragonite, phengite and clinozoisite are alteration products of primary plagioclase and paragonite, whereas pargasitic amphibole is replaced by chlorite and pumpellyite.

Detrital boulder CU22 is a foliated tonalitic rock composed of strongly retrogressed magmatic plagioclase, quartz, epidote, rutile and apatite. The zircon is clear to pinkish, mostly stubby or fragmented, rarely prismatic, and display well-developed magmatic oscillatory zoning (Fig. 4). No core–rim relationships were observed in CL images. The magmatic mineral assemblage is strongly overprinted by albite, clinozoisite–epidote, white mica (paragonite and phengite), chlorite and titanite. Primary plagioclase is largely transformed to albite, clinozoisite, paragonite-phengite and cryptocrystalline material (saussurite). Epidote and white mica form aggregates aligned parallel to the foliation. Patches of retrograde chlorite follow the foliation. These primary and overprinting assemblages are consistent with those of other tonalitic-trondhjemitic rocks from the Sierra del Convento mélange.

Mineral compositions

Amphibole

Amphibole in the studied samples covers a wide range of compositions (Fig. 5). The prograde grains from the amphibolites display a faint concentric zoning with

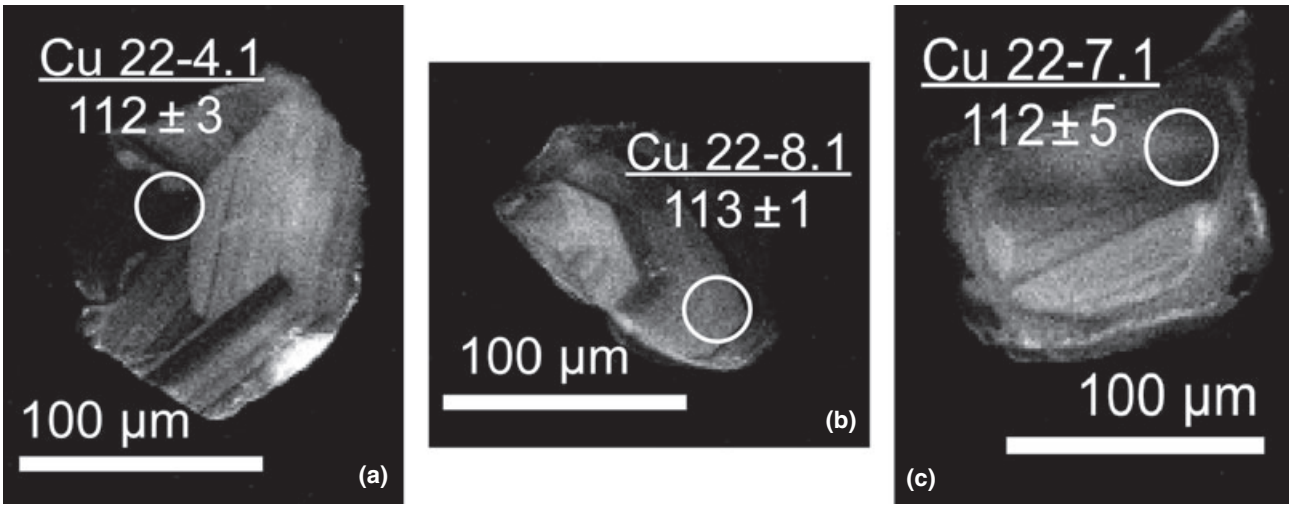

Fig. 4. CL images of zircon from tonalitic sample CU22 showing oscillatory zoning typical of magmatic zircon, location of analyses, and ages (see Table 2).

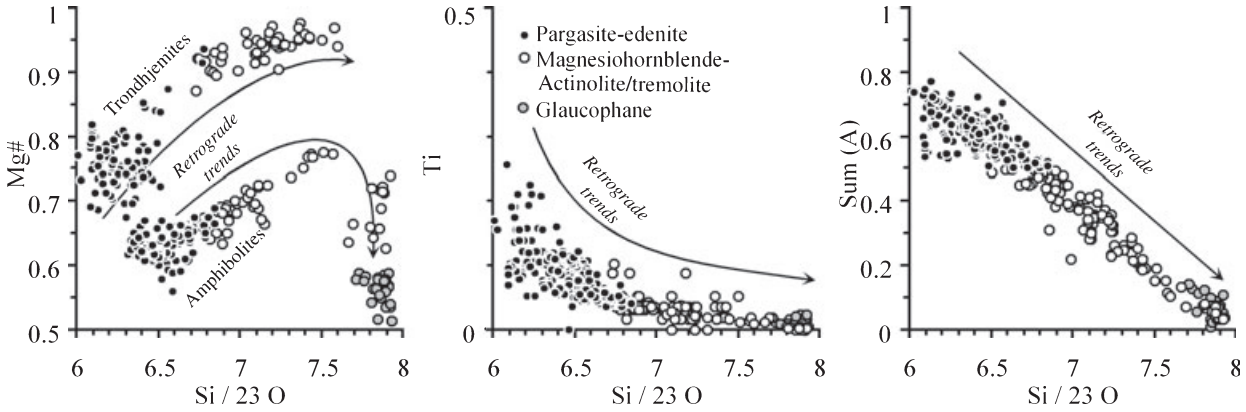

Fig. 5. Compositional plots of Mg, Ti, sum(A) *v.* Si of calcic and sodic amphiboles from trondhjemitic and amphibolitic samples, with indication of retrograde trends for calcic amphibole.

cores of edenite and outer shells of pargasite bearing higher Na-in-A, total Al and Ti and lower Si, Na-in-B and Mg# than the cores. This trend correlates with the composition of amphibole inclusions within garnet that ranges from edenite to pargasite. As a whole, this indicates prograde growth and peak compositions of pargasite. Retrograde overprinting developed patches of Ti-poor edenite and magnesiohornblende compositions within the primary pargasitic grains. These patches have tiny inclusions of rutile/titanite likely formed after 'exsolution' from Ti-rich primary pargasitic compositions. Post-peak overprints at the rims of the prograde grains consist of edenite, magnesiohornblende and actinolite. The trend involves a decrease in Na-in-A, total A and Ti and an increase in Si and Mg#, though the latest actinolitic products show a back decrease in Mg# as Si increases (Fig. 5). Retrograde glaucophane shows a more restricted range of compositional variations (Fig. 5).

Magmatic amphibole in the trondhjemites is pargasitic and similar to that of metamorphic peak amphibole from the amphibolites, except for being higher in Mg# as a consequence of a bulk-rock composition effect (García-Casco *et al.*, 2008a). It shows no discernible growth zoning though the grains are overprinted by retrograde edenite, magnesiohornblende and tremolite developed as patches and along fractures, exfoliation planes and the crystal rims. As in the amphibolites, the retrograde trend involves a decrease in Na-in-A, total Al and Ti and an increase in Si and Mg#, though no decrease in Mg# was detected in the youngest tremolitic compositions (Fig. 5). Glaucophane is not present as a retrograde product in the trondhjemites.

Garnet

Garnet is relatively rich in almandine, intermediate in grossular and pyrope, and poor in spessartine (Fig. 6). Growth zoning is faint, with cores richer in spessartine and rims richer in Mg# denoting prograde growth (Figs 3c & 5). Faint prograde zoning and the lack of low-temperature phases included within garnet suggest

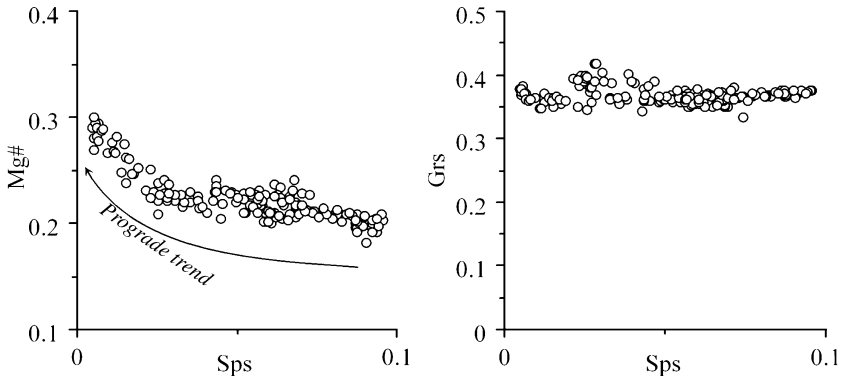

Fig. 6. Compositional plots of Mg and Grs *v.* Sp of garnet from amphibolites, with indication of the prograde trend.

growth close to peak conditions during prograde metamorphism (García-Casco *et al.*, 2006, 2008a). Retrograde readjustments are noted by an increase in Mn and decrease in Mg# at the rims and along fractures traversing the grains where retrograde magnesiohornblende-actinolite, glaucophane, chlorite, pumpellyite, phengite and/or albite are observed.

Epidote

Epidote has low Fe^{3+} contents in the amphibolite samples, with pistacite contents ($X_{Ps} = Fe^{3+}/[(Al-2) + Fe^{3+}]$) ranging from 0.04 to 0.17. No distinctive zoning was detected in the studied amphibolite samples. Epidote in the trondhjemite samples shows larger compositional variations. The Fe^{3+} contents are higher in the medium-grained idiomorphic (magmatic) crystals whereas near-clinozoisite compositions in the retrograde grains formed after plagioclase breakdown (X_{Ps} up to 0.56 and down to 0.04 respectively). Magmatic crystals show patchy zoning, with irregular distribution of Fe^{3+}.

Plagioclase

Plagioclase in the amphibolites is retrograde and almost pure albite in composition (X_{Ab} = 0.92–1.0). The composition in the trondhjemites is more varied (X_{Ab} = 0.71–1.0) as a result of magmatic crystallization and late overprinting and growth. The magmatic compositions are richer in Ca, whereas retrograde overprints trend towards albite. The maximum X_{An} recorded in the studied samples are 0.29 (CV228c), 0.19 (CV53f), 0.11 (CV227b) and 0.98 (CU22). Although these compositions were identified with the aid of XR and BSE images, they do not necessarily represent the original magmatic composition of plagioclase. It is inferred that the maximum X_{An} recorded (in CV228c) is closer to the original composition of magmatic plagioclase of all the samples.

Paragonite

Paragonite covers a wide range of compositions as a result of magmatic crystallization as well as late overprinting and growth (Fig. 7; see also García-Casco, 2007). Magmatic crystals have high K and moderate to high Ca contents. The maximum K and Ca contents are recorded in sample CV53f (0.41 & 0.28 apfu, respectively), although in this and other samples the highest Ca contents do not correlate with the highest K contents (García-Casco, 2007; García-Casco *et al.*, 2008a). Retrograde grains replacing magmatic plagioclase approach the paragonite end-member.

Phengite

Phengitic mica in amphibolite CV139a shows a wide spectrum of compositions (Fig. 7). Si and Ti contents range from 6.34 to 7.01 and 0.00 to 0.08 apfu, respectively. Medium-grained crystals show complex irregular zoning, but the areas with lower Si and higher Ti, considered to have formed at higher temperature, are preferentially distributed in cores. These less silicic compositions are rich in Ba, amounting to up to 0.13 apfu. The latest retrograde grains of phengite are commonly associated with retrograde actinolite, glaucophane, chlorite and pumpellyite in fractures and replacing other minerals, and show the largest Si, Fe and Mg and the lowest Ba contents (down to 0.02 apfu). The composition of retrograde phengite in the trondhjemites is similar to that of retrograde phengite in amphibolite sample CV139a (Fig. 7). Si contents are up to 7.05 apfu and Ti and Ba contents are low (up to 0.03 and 0.02 apfu, respectively).

Other minerals

Chlorite in the amphibolites is retrograde, and has Al = 4.75–4.99 apfu, Mn = 0.03–0.12 apfu and Mg# ($Fe^{2+} = Fe_{total}$) = 0.42–0.63. Chlorite in the trondhjemites is retrograde and similar in composition to that in the amphibolites, except for being more magnesian (Mg# = 0.68–0.80).

Pumpellyite in the amphibolites is retrograde and has Mg# ($Fe^{2+} = Fe_{total}$) = 0.56–0.71, whereas it is more magnesian in trondhjemites and has Mg# ($Fe^{2+} = Fe_{total}$) = 0.70–0.83. Titanite has Al up to 0.06 apfu. Relict magmatic kyanite (in CV53f) and

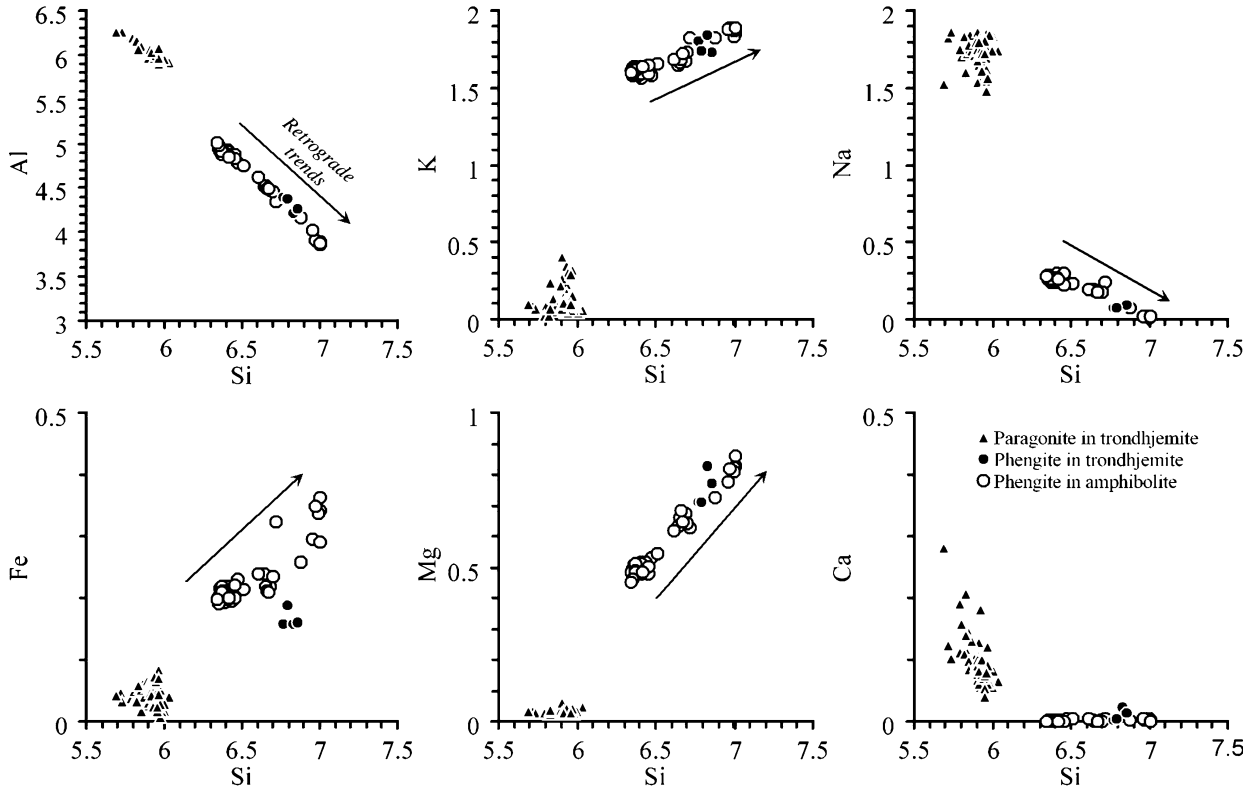

Fig. 7. Compositional plots of Al, K, Na, Fe, Mg & Ca *v.* Si of paragonite and phengite from trondhjemitic and amphibolitic samples, with indication of the retrograde trend of phengite.

retrograde lawsonite (in CV228c) are almost pure in composition.

P–T CONDITIONS AND PATHS

P–T conditions

Temperatures and pressures were estimated following the optimal *P–T* method of Powell & Holland (1994) using THERMOCALC (Holland & Powell, 1998; version 3.25, dataset 5.5, 12 November 2004). Calculations were performed using different combinations of phases grown during pre-peak, peak and post-peak conditions, as described below for each sample. An H_2O-fluid was included in all assemblages. All calculations are based on a number of independent reactions. The activities and (1σ) activity uncertainties of each end-member included in the calculations were obtained with the software AX (T.J.B. Holland & R. Powell, unpublished data). The *P–T* uncertainties (σT and σP) given represent $\pm 1\sigma$. The correlation between σT and σP for a given calculation is given below as 'corr'. High correlation indicates that with aT (or P) the other value is well constrained. Thus, large σT and σP imply well-constrained *P–T* data if the former are highly correlated. The σT and σP uncertainties and correlations are appropriately incorporated into the uncertainty ellipses of Fig. 8 calculated following Powell & Holland (1994). The calculations of pre-peak and peak conditions passed the 'sigfit' test for statistical consistency, but some of the calculations of magmatic and retrograde conditions did not pass this test, suggesting equilibrium problems. The test implies that the 'sigfit' values (quoted below for each calculation) should approach unity (for further details, see Powell & Holland, 1994).

Amphibolites

The calculated pre-peak and peak *P–T* conditions are based on the inclusion and matrix assemblage Grt + (edenite-pargasite)Amp + Ep + H_2O, whereas the retrograde conditions were calculated using actinolitic Amp + Gl + Chl + Ep + Grt(retrograded rims) + Ab + H_2O. For sample CV230b, calculated peak and retrograde conditions were 708 ± 69 °C/13.8 ± 2.2 kbar (corr 0.455, sigfit 0.81) and 472 ± 21 °C/10 ± 1 kbar (0.473, 1.48) respectively (García-Casco *et al.*, 2008a). For sample CV139a, the calculated peak and retrograde conditions are 719 ± 37 °C/16.2 ± 1.8 kbar (0.353, 0.83) and 383 ± 57 °C/8.9 ± 1.8 kbar (0.921, 1.46), respectively.

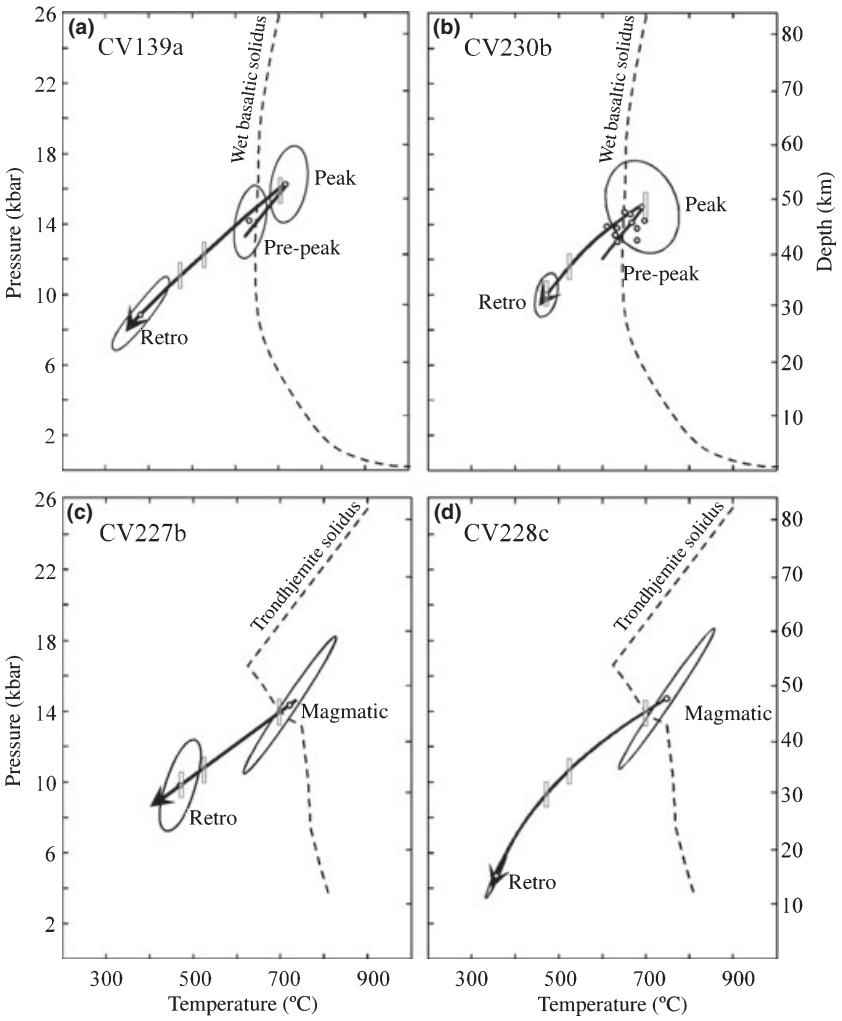

Fig. 8. *P–T* paths of studied samples showing conditions calculated following the average *P–T* method of Powell & Holland (1994) using software THERMOCALC (error ellipses: $\pm 1\sigma$). The reference temperatures for age determinations at 700 °C (zircon crystallization), 525 °C (pargasite cooling), and 465 °C (retrograde amphibole overprints) are indicated. The wet-basalt solidus of Vielzeuf & Schmidt (2001) is included in (a) and (b); and the trondhjemite solidus for a representative sample from the Sierra del Convento mélange (García-Casco, 2007) is included in (c) and (d).

Trondhjemites

Because of the widespread retrograde overprinting of magmatic plagioclase that is transformed to albitic compositions (+paragonite + clinozoisite), the conditions of magmatic crystallization for these samples are uncertain. For each sample, the analyses which most closely approach the composition of the original magmatic plagioclase are those with the highest Ca contents. Nevertheless, there is no guarantee that these analyses effectively correspond to the original compositions of magmatic plagioclase.

The magmatic *P–T* conditions calculated for sample CV228c and based on the assemblage Amp + Ep + high-K Pa + Qtz + high-Ca Pl (+H_2O) are 747 ± 88 °C/14.7 ± 3.2 kbar (0.988, 0.95) (García-Casco *et al.*, 2008a), and overlap with the peak *P–T* conditions calculated for the amphibolites. Retrograde conditions of 356 ± 18 °C/4.7 ± 1 kbar (0.963, 0.31) were calculated in this sample using tremolitic Amp + Chl + Ep + low-K Pa + Lws + Qtz + Ab + H_2O.

The magmatic conditions for all other trondhjemite samples could not be calculated with confidence. Even if spot analyses of relict plagioclase with the highest Ca content from individual samples are used, the calculations (based on the same magmatic assemblage as CV228c) yield discordant high pressures of ~20 kbar and large associated errors, as a consequence of using non-equilibrium plagioclase compositions (cf. García-Casco *et al.*, 2008a). Using the composition of plagioclase with the highest-Ca content from sample CV228c, the calculated peak conditions for sample CV227b are 721 ± 84 °C/14.3 ± 3.1 kbar (0.987, 0.59), consistent with peak conditions of the amphibolites. For this sample, the calculated retrograde conditions (assemblage tremolitic Amp + Chl + Ep + low-K Pa + Qtz + Ab + H_2O) are 472 ± 38 °C/9.8 ± 2.1 kbar (0.643, 1.93).

P–T paths

The calculated *P–T* conditions indicate that the amphibolites experienced peak metamorphic conditions

corresponding to the epidote–amphibolite facies at 14–16 kbar and 700 ± 50 °C. The prograde *P–T* paths of the amphibolites reached conditions above the wet-solidus of (MORB-like) basaltic composition (Fig. 8), appropriate for the generation of trondhjemitic liquids at high pressure. Crystallization of these magmas occurred at ~14–15 kbar. The retrograde mineral assemblages in all rock types indicate blueschist facies overprints at variable *P–T* (8–10 kbar/380–470 °C). This indicates cooling at relatively high pressure and counterclockwise *P–T* paths, in agreement with previous proposal by García-Casco *et al.* (2006, 2008a).

GEOCHRONOLOGY

SHRIMP zircon dating

Eight single zircon grains from a trondhjemite boulder (CU22) produced a well-defined cluster of concordant results (Table 2), with a mean $^{206}Pb/^{238}U$ age of 112.8 ± 1.1 Ma (Fig. 9). Grain 7 (Table 2) is low in U (68 ppm) and therefore has a relatively large error in the isotopic ratios and age. The data are graphically presented in the conventional Concordia plot in Fig. 9. As partial melting of parental amphibolite occurred at ~700 ± 50 °C, the above pooled age reflects the time of zircon crystallization upon cooling of the tonalitic melt at ~700 °C.

$^{40}Ar/^{39}Ar$ amphibole dating

The Ar/Ar isotopic data (Table 3) are graphically shown in Figs 10 & 11.

Amphibolites

In sample CV139a the brown amphibole concentrate (i.e. peak pargasite) displays a slightly disturbed staircase-type pattern. Steps 4–8 together constitute 93.3% of the ^{39}Ar released and yielded an integrated age of 96.5 ± 0.8 Ma (Fig. 10a). The isochron correlation age (i.c.a.) of all steps of hornblende, equally weighted according to model 2 in the software ISOPLOT/EX (Ludwig, 2001), is 93.9 ± 2.4 Ma, with a $^{40}Ar/^{36}Ar$ intercept at 283 ± 3.5 (Fig. 10b), which is close to the atmospheric value of 295.5. Interestingly, the K/Ca ratio (the inverse of the $^{37}Ar/^{39}Ar$ ratio) is increasing from step 1 to 8 of the brownish amphibole arguing for a higher K/Ca ratio in the core of brownish amphibole grains. The green amphibole concentrate (i.e. retrograde calcic amphibole), on the other hand, shows a pattern with slight variation and excess Ar in the first two steps. Steps 4–7 define a plateau age of 82.67 ± 0.84 Ma, comprising 69.9% of the ^{39}Ar (Fig. 10c). The isotopic correlation age of this amphibole concentrate, all steps included, gives an age of 81.2 ± 5.6 Ma with a $^{40}Ar/^{36}Ar$ intercept at 291.8 ± 8.1 (Fig. 10d). For steps 3–7, the calculated isochron age is 82.4 ± 3.1 Ma ($^{40}Ar/^{36}Ar$ intercept at 288.5 ± 5.8). The K/Ca ratio in the green amphibole is lower than in brownish amphibole of the same sample.

The integrated age of 96.5 ± 0.8 Ma of the brown amphibole concentrate represents cooling of peak pargasitic amphibole through the appropriate argon retention temperature (see below). The plateau age of 82.67 ± 0.84 Ma of the green amphibole concentrate reflects retrograde growth or cooling of retrograde amphibole through the appropriate argon retention temperature. Thereby, these ages date cooling in the sample after peak metamorphism.

Amphibole from sample CV230b yielded a disturbed pattern with excess Ar in the first step. The isochron age for all steps of hornblende is 80.5 ± 8.4 Ma with a $^{40}Ar/^{36}Ar$ intercept at 296 ± 15 (Fig. 10f). Calculation of an integrated age for steps 3–8, comprising 97.5% of the ^{39}Ar released, yielded 90.6 ± 1.1 Ma. As the dated amphibole concentrate contains mixed grains of peak (brown) pargasitic amphibole and green retrograde amphibole, following the results of sample CV139a, this age can be interpreted as a mixing age of two components. On the one side, steps 3, 4 and 8, comprising 71.4% of the ^{39}Ar released, yield an integrated age of 86.9 ± 0.9 Ma that reflects growth/cooling of retrograde calcic amphibole contained in the concentrate, whereas steps 5–7, comprising 26.1% of the ^{39}Ar released, yield an integrated age of 100.6 ± 1.8 Ma (Fig. 10e) that reflects the maximum age of cooling of peak (brown) pargasitic amphibole.

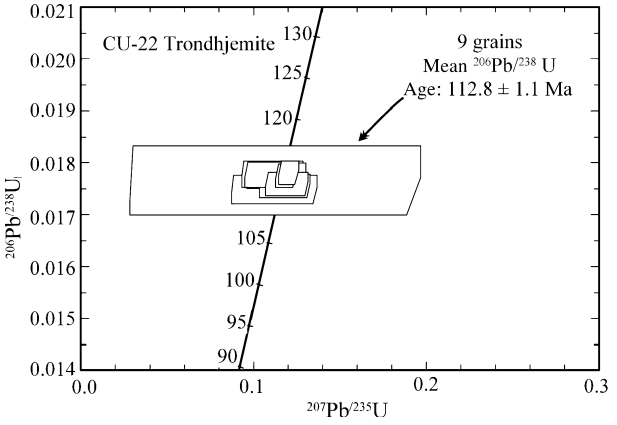

Fig. 9. Concordia diagram showing SHRIMP analyses of zircon from a tonalitic boulder in the Yacabo River. Isotopic ratios are radiogenic. Data boxes for each analysis are defined by standard errors (1σ) in $^{207}Pb/^{235}U$, $^{206}Pb/^{238}U$ and $^{207}Pb/^{206}Pb$.

Trondhjemites

Amphibole from sample CV227b yielded a slightly disturbed pattern with excess Ar in the first three steps. The integrated age is 94.7 ± 1.1 Ma and covers 97.7% of the ^{39}Ar released. The age of the last step (step 9) is 97.7 ± 0.9 Ma and comprises the highest percent of the ^{39}Ar released (41.6%) (Fig. 11a). The disturbed

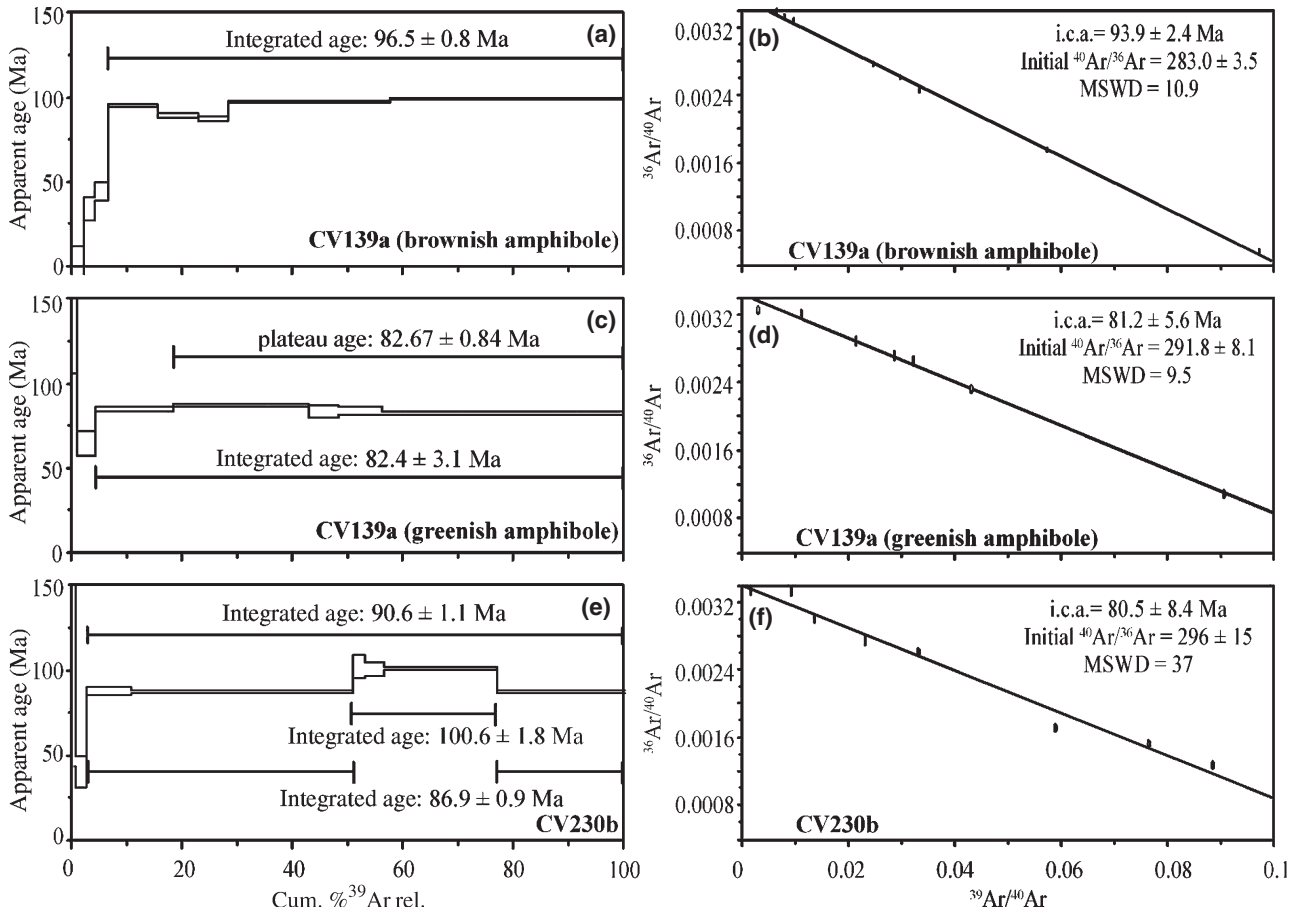

Fig. 10. Incremental step-heating analyses of amphibole from amphibolite samples CV139a (brownish and greenish amphibole) & CV230b. Rectangle heights and all errors are 1σ.

pattern reflects the effects of retrograde overprinting of magmatic pargasite. Hence, the integrated age of 94.7 ± 1.1 Ma is a mean of the cooling age of magmatic crystals and growth of retrograde amphibole. The age of cooling of pargasite is taken as 97.7 ± 0.9 Ma, but the pattern of this sample does not allow us to decipher the age of retrograde growth/cooling of calcic amphibole.

A similar picture arises from samples CV228c & CV53f. Amphibole from sample CV228c yielded a disturbed argon-release pattern with excess argon in the first three steps. The age of the last step, which comprises 29% of the ^{39}Ar released, is 105.5 ± 1.9 Ma. Steps 4–7 comprise 67.9% of the ^{39}Ar released and yielded an integrated age of 85.7 ± 1.5 Ma (Fig. 11c). Following results from other samples, these two ages represent the maximum age of cooling of magmatic pargasitic amphibole and the age of growth/cooling of retrograde amphibole, respectively.

The amphibole concentrate of sample CV53f also yielded a disturbed argon-release pattern with excess Ar in the first five steps which comprise 2.6% of the ^{39}Ar released. Steps 6–10, comprising 97.4 of the ^{39}Ar released were used for calculation of an integrated age of 94.8 ± 2.3 Ma (Fig. 11e), that reflects a mean age of cooling of magmatic pargasite and of overprinting retrograde amphibole. Steps 9–10, comprising 42.2% of ^{39}Ar released yielded an integrated age of 103.6 ± 2.6 Ma (Fig. 11e). The higher ^{39}Ar percent released during step 7 (42.8%) yielded an age of 87.1 ± 0.9 Ma (Fig. 11e). These two ages represent the maximum age of cooling of magmatic pargasitic amphibole and the age of the overprinting by retrograde amphibole, respectively.

In summary, Ar/Ar dating results from all samples indicate two distinct groups of ages reflecting cooling events in the studied rocks. The first group, 106–97 Ma (average = 100.8 Ma), represents cooling of peak/magmatic amphibole through the appropriate argon retention temperature of amphibole. The second group of ages, 87–83 Ma (average = 85.6 Ma), represents growth/cooling of retrograde calcic amphibole overprinting peak/magmatic pargasitic amphibole.

DISCUSSION

To evaluate the age data in the context of the thermal history of the studied rocks, the shape of the *P–T* paths

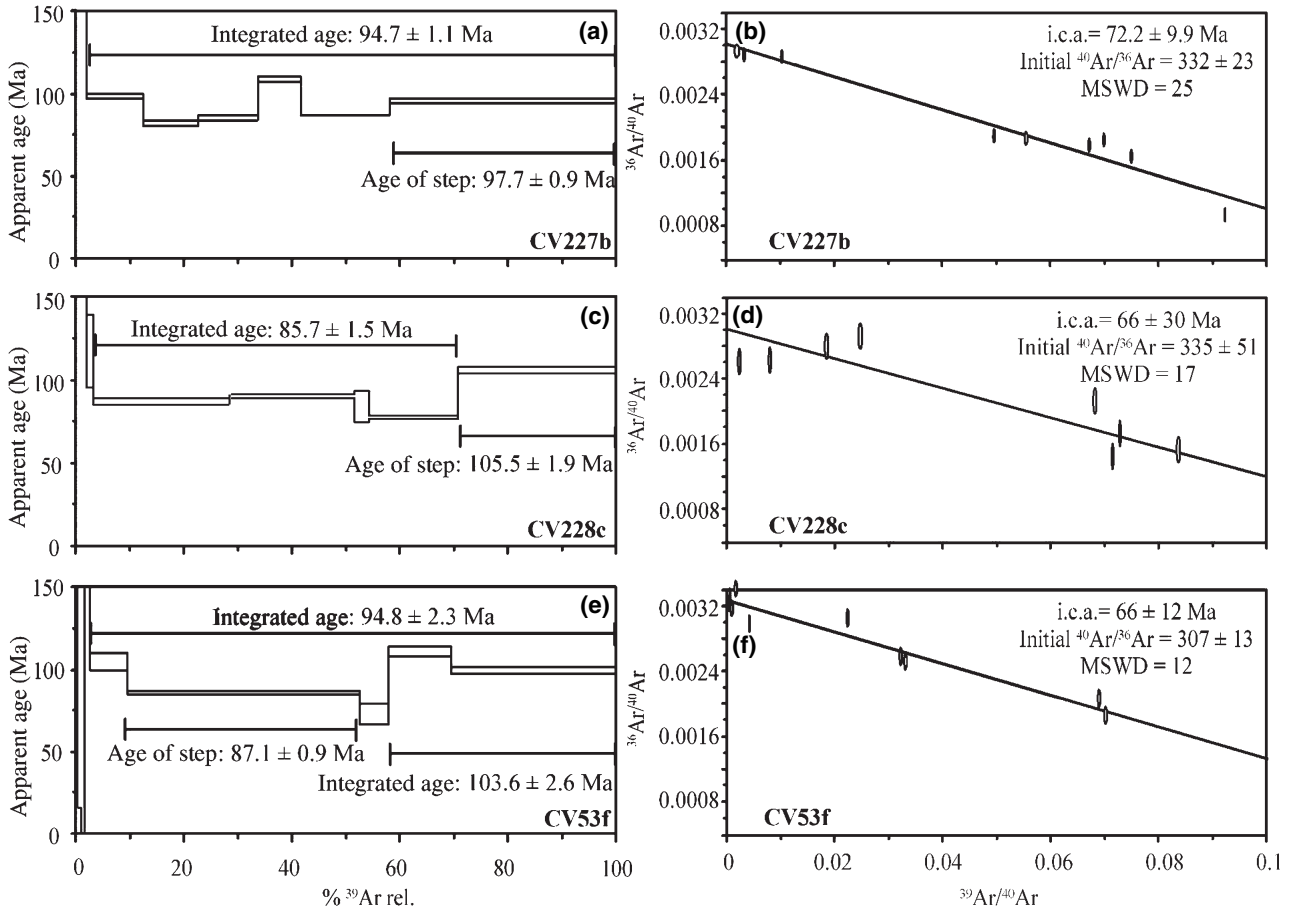

Fig. 11. Incremental step-heating analyses of amphibole from the trondhjemite samples CV227b, CV228c & CV53f. Rectangle heights and all errors are 1σ.

must be known. These shapes are, however, uncertain because only two calculated *P–T* points constrain their retrograde paths. Near-linear fits, as those presented in Fig. 8, would indicate cooling and decompression since the beginning of accretion of the blocks to the overriding plate. However, there are a number of arguments against the retrograde *P–T* paths being nonlinear.

Petrological arguments, thermobarometric calculations and phase relations (see García-Casco *et al.*, 2006, 2008a; García-Casco, 2007) allow the conclusion that the onset of retrogression was characterized by near-isobaric cooling, followed by cooling and decompression. Furthermore, as discussed by these authors and below, the blocks of the mélange formed in a nascent subduction environment. Geophysical (Gerya *et al.*, 2002) and geochemical (Perchuk *et al.*, 1999) modelling indicate that retrograde *P–T* paths of rocks formed in this environment are characterized by a first stage of near-isobaric cooling at high pressure, followed by a second stage of exhumation characterized by decreasing pressure and temperature. Following the results of these models, the first stage is developed once the blocks are accreted to the (essentially anhydrous) upper plate mantle, whereas the second stage is developed once a serpentinitic subduction channel is formed upon hydration of the upper plate mantle, allowing upward flow of the blocks. A similar multistage *P–T* path has recently been deduced by Krebs *et al.* (2008) in contemporaneous (*c.* 103 Ma) eclogite blocks in the Rio San Juan complex (Dominican Republic), formed in the same subduction environment as the Cuban Sierra del Convento amphibolites and trondhjemites (García-Casco *et al.*, 2008a).

Consequently, the studied samples followed similar multistage *P–T* paths. Because all studied samples attained similar *P–T* during peak metamorphic/magmatic conditions and retrogression, the following discussion is developed considering a single retrograde multistage *P–T* path for all the studied rocks (Fig. 12). In addition, a previous subduction stage will be considered for the amphibolites.

Temperature–time path

The calculated peak/magmatic conditions in the amphibolites and trondhjemites suggest that the onset

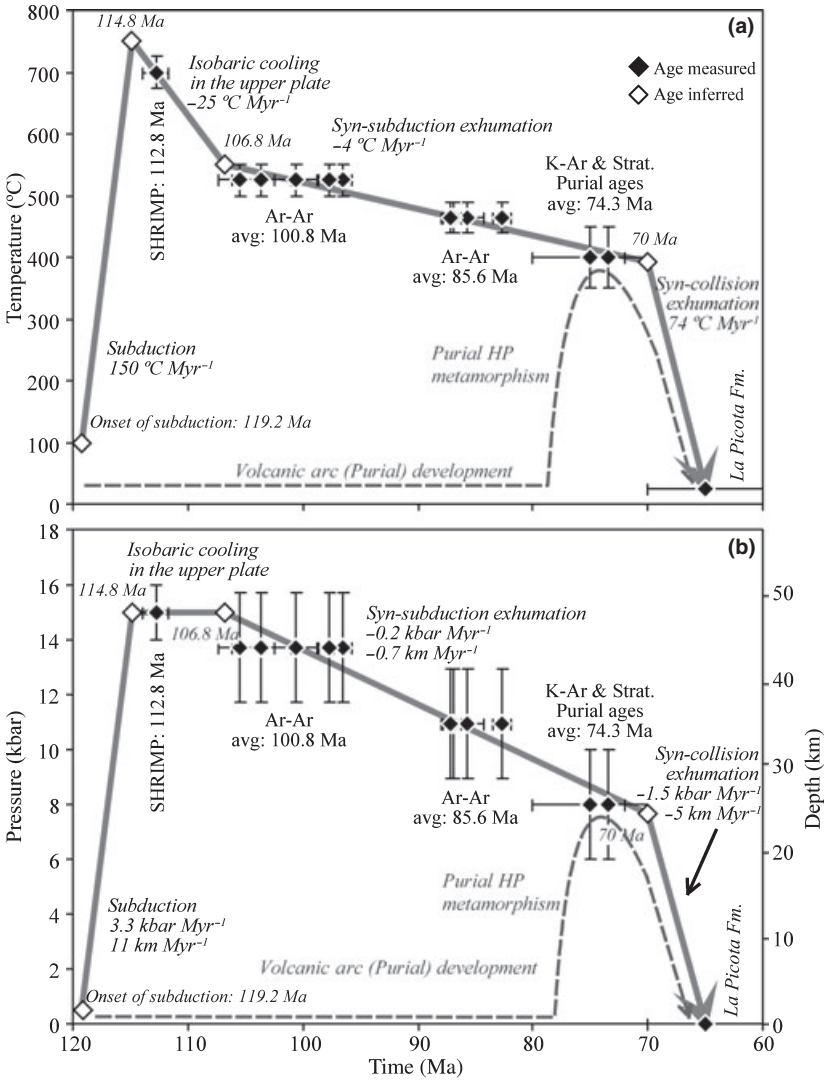

Fig. 12. (a) *T–t* and (b) *P–t* paths derived from geochronological and petrological data of the Sierra del Convento mélange and neighbouring geological bodies. See text for construction of the model paths. Schematic *T–t* and *P–t* paths of the Cretaceous Volcanic Arc Purial complex is shown for reference.

of the isobaric cooling section of the retrograde *P–T* paths occurred at ~15 kbar, 750 °C. However, the age of this *P–T* point is not known. Based on the crystallization age of zircon, the onset of cooling should have occurred before *c*. 113 Ma. Similarly, the temperature and age of the low-*T* end of the isobaric path are not known. Both must be estimated indirectly. This can be done by extrapolating the *T–t* data of the two distinct groups of geologically significant Ar/Ar ages in the studied rocks (Fig. 12a).

The closure temperature (T_c) for the Ar/Ar system in hornblende depends on a number of factors including the cooling rate, the effective diffusion, grain size and chemical compositions (e.g. Harrison, 1981; Dahl, 1996). In general, 480–580 °C is agreed as the appropriate T_c for cooling rates of 5–1000 °C Myr^{-1} (Harrison, 1981). Baldwin *et al*. (1990) calculated a lower T_c for metamorphic hornblende than for Ti-richer igneous hornblende assuming the same cooling rate. Moreover, Dahl (1996) indicated that the closure temperature for Mg-rich clinoamphibole is 60 ± 10 °C higher than for their Fe-rich analogues, and 40 ± 15 °C higher for amphibole with full A-site occupancy relative to those with empty A-sites. Following these results, the closure temperature of our Ti- and A-site-richer pargasitic amphibole should be relatively high, and an average T_c of 525 °C is selected. This temperature was achieved by the studied rocks during the period 106–97 Myr. The youngest group of Ar/Ar amphibole ages (87–83 Ma) must be interpreted in terms of retrograde overprinting. These ages may either correspond to the formation of retrograde amphibole, to cooling of these overprints through their appropriate argon retention temperature, or both. Following the findings of other authors quoted above, an average temperature of 465 °C has been selected for this event, although a range probably would be more appropriate because of the heterogeneous edenite-magnesiohornblende-actinolite/tremolite composition (and hence timing of crystallization age) of the overprints. To further constrain the *T–t* data set,

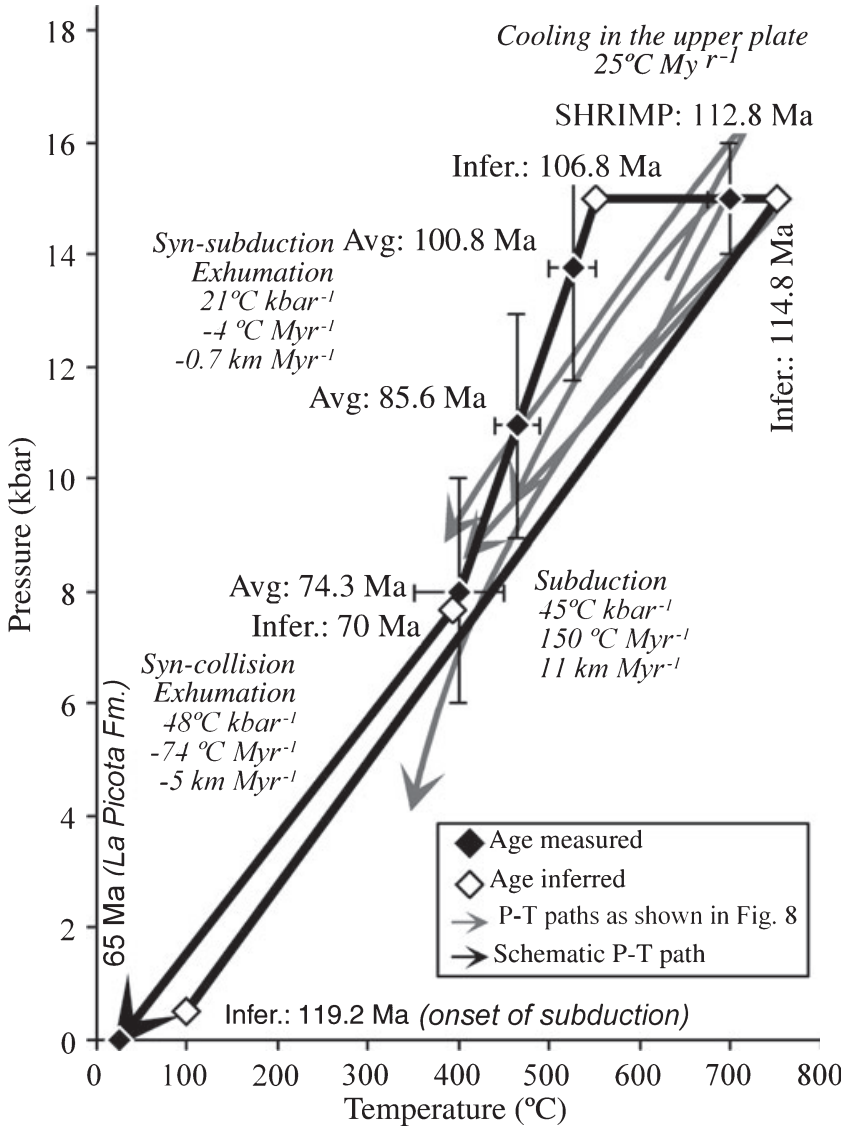

Fig. 13. Model multistage *P–T–t* path for the studied rocks including the subduction, cooling in the upper plate, syn-subduction exhumation, and syn-collision exhumation stages, measured and inferred *P–T–t* conditions and rates.

the timing of blueschist metamorphism in the underlying Purial volcanic arc complex has also been taken into account. A schematic *T–t* path for the Purial complex is indicated in Fig. 12a. The available data indicate that metamorphism occurred at *c.* 75 Ma (75 ± 5 Ma, K-Ar whole-rock, Somin *et al.*, 1992; and 75–72 Ma, based on stratigraphic-palaeontological arguments, Iturralde-Vinent *et al.*, 2006). No *P–T* data are available for the sample dated by Somin *et al.* (1992). Similar blueschist rocks in the complex yield a range of *P–T* values of 300–450 °C and 5–10 kbar (A. García-Casco, unpublished data). Based on this range, we have approximated the metamorphic conditions of the sample dated by Somin *et al.* (1992) as 400 °C and 8 kbar (Fig. 12a).

Using a linear regression on the aforementioned *T–t* data (Fig. 12a), the extrapolation to temperatures higher than 525 °C (first group of Ar/Ar ages) indicates that the low-*T* end of the isobaric cooling stage cannot be higher than 575 °C. If it was, the extrapolated ages would be older than the crystallization age of zircon at 700 °C. Consequently, we have chosen 550 °C for the low-*T* end of the isobaric cooling stage. This temperature is consistent with calculations of Perchuk *et al.* (1999), Gerya *et al.* (2002) and Krebs *et al.* (2008). The calculated age for this temperature is 106.8 Ma using the linear regression on the Ar/Ar and K/Ar *T–t* data (Fig. 12a). The same technique was used to calculate the age of the high-*T* end of the isobaric cooling stage (i.e. the age of peak-*T*). A linear *T–t* regression was calculated using the low-*T* end of the isobaric cooling stage and the conditions of zircon crystallization at 112.8 Ma, 700 °C. The calculation gives 114.8 Ma for peak-*T* (i.e. the high-*T* end of the isobaric cooling stage) of 750 °C. The two stages thus calculated are denoted as the cooling in the upper plate and cooling in the subduction channel stages, respectively (Fig. 12a).

The exposure of the ophiolites and volcanic arc complexes of the region is indicated by the age of the syn-orogenic Mícara-La Picota Formations (68–63 Ma). Linear extrapolation of the syn-subduction exhumation *T–t* path to ages younger than the metamorphic ages of the Purial complex indicates that an inflexion must occur in the *T–t* path to accommodate the age of surface exposure of the complexes. The *T–t* data suggest inflexion at *c*. 70 Ma, for which a temperature of 394 °C was calculated by linear extrapolation of the syn-subduction exhumation *T–t* path. A *T–t* section was calculated for the final cooling stage, denoted here the syn-collision stage, with these data and an average age of 65 Ma for the timing of surface conditions at 25 °C (La Picota Fm.) (Fig. 12a).

Finally, the onset of the subduction stage of the amphibolites has been determined following the calculations of Krebs *et al*. (2008) for the initial stages of subduction in the region. These authors suggested a convergence rate of 30 km Myr^{-1} and a burial rate of 11 km Myr^{-1}. Pre-subduction conditions of 0.5 kbar and 100 °C for the oceanic crust represented in the Sierra del Convento and linear burial and heating to 750 °C, 15 kbar yield an age of 119.2 Ma for the onset of subduction of the amphibolite blocks (Fig. 12a). Different burial rates would, of course, result in varying ages for the onset of subduction. For 22 and 5.5 km Myr^{-1}, the resulting ages are 117 and 124 Ma, respectively.

Pressure–time and pressure–temperature paths

The data and calculations presented above can be extended to calculate *P–t* and *P–T* paths (Figs 12b & 13). However, before this is done the pressures corresponding to the two groups of Ar/Ar ages must be deduced. As a first approximation, it has been assumed that each group of ages corresponds to a distinct pressure along an average *P–T* path. These two pressures were calculated using a linear *P–T* regression including the points representing the lower-*T* limit of the isobaric cooling path (i.e. 15 kbar, 550 °C), an estimate of 450 °C, 10.3 kbar for the calculated retrograde conditions, and the estimated *P–T* data for the sample dated by Somin *et al*. (1992) of the Purial complex. Using this equation, the pressures calculated for cooling of pargasite (at 525 °C) and growth/cooling of retrograde calcic amphibole (at 465 °C) are 14 and 11 kbar, respectively.

With these data and those given in the temperature–time section, the schematic *P–t* and *P–T* paths were constructed, including: (i) the subduction; (ii) cooling in the upper plate; (iii) syn-subduction; and (iv) syn-collision stages (Figs 12b & 13).

Heating/cooling and burial/exhumation rates

Although the *P–T–t* paths of subducted rocks that return to the surface are highly variable (Gerya *et al*., 2002), our schematic *P–T–t* path compares well with predicted and observed paths of oceanic material subducted during the initial stage and accreted to the hangingwall at great depth. For this type of material subducted under a constant and moderate convergence rate of 30 km Myr^{-1} (Gerya *et al*., 2002), calculated maximum burial and heating rates are 15–20 km Myr^{-1} and 150–250 °C Myr^{-1}, respectively, which compare well with our model average burial and heating rates or 11 km Myr^{-1} and 149.4 °C Myr^{-1}, respectively. In calculations developed by Gerya *et al*. (2002), accretion to the upper plate mantle occurs within a few million years after onset of subduction (at *c*. 6.5 vs. 4.3 Ma in our model *P–T–t* path), the residence time in this environment is *c*. 9 Myr (vs. our 8 Myr), and the near-isobaric cooling rates are 0–30 °C Myr^{-1} (vs. our average 25 °C Myr^{-1}). Onset of return flow occurs 15.5 Myr after the onset of subduction (vs. our 12.4 Myr). This time marks the formation of the subduction channel (i.e., melange) by hydration (serpentinite formation) of the upper plate mantle (at ~550 °C). As calculated by Gerya *et al*. (2002), the exhumation and cooling rates during the return flow in the subduction channel are much lower than the burial and heating rates. This observation is in agreement with our linear model calculations for the syn-subduction stage of 0.7 km Myr^{-1} and 4 °C Myr^{-1}, respectively, which compare well with the rates calculated for blocks from other mélanges elsewhere which are considered to have formed in subduction channels (Reiners *et al*., 2002; Anczkiewicz *et al*., 2004; Wallis *et al*., 2004; Krebs *et al*., 2008).

Our schematic *P–T–t* path includes a final stage related to collision in the region (García-Casco *et al*., 2008b), a situation not modelled by Gerya *et al*. (2002). The linear model calculations for this collision stage suggest exhumation and cooling rates of 5.1 km Myr^{-1} and 73.7 °C Myr^{-1}, respectively. These rates are 8 and 17 times higher, respectively, than those calculated for the syn-subduction exhumation stage. This result is in agreement with estimates of fast exhumation rates greater than 1 km Myr^{-1} caused by buoyancy and/or normal faulting and/or extrusion wedge processes in collision environments (e.g. Monié *et al*., 1994; Duchêne *et al*., 1997; Rubatto & Hermann, 2001; Ring & Reischmann, 2002; Baldwin *et al*., 2004).

Interpretation of previous geochronology

Our schematic *P–T–t* path for the Sierra del Convento amphibolites and trondhjemites allows the significance of previously published age data to be assessed. These data were published without appropriate consideration of the *P–T* path followed by the rocks (Hatten *et al*., 1989; Somin *et al*., 1992; see also Millán, 1996).

Somin & Millán (1981), Hatten *et al*. (1989) and Somin *et al*. (1992) provided K-Ar (whole-rock, hornblende and paragonite) ages for garnet-amphibolites and trondhjemite ranging from 116 ± 9 to

82.2 ± 2.5 Ma. Somin *et al.* (1992) noted that the quoted ages are probably too high because of excess argon. In the light of our new Ar/Ar results, however, these data must be considered as indications of the timing of cooling and retrograde overprinting rather than of peak metamorphism. The oldest K-Ar age of 116 ± 9 Ma provided by Hatten *et al.* (1989) and Somin *et al.* (1992) correspond to an amphibole separate from garnet amphibolite. This age should now be interpreted as an imprecise indication of cooling of high-grade pargasite ('carintine', as described by Somin *et al.*, 1992).

Hatten *et al.* (1989) also provided imprecise zircon U-Pb ages of 126–120 and 105–103 Ma from a banded zoisite-rich rock ('zoisitite', as described by Millán, 1996), and interpreted these as ages of the protolith and its metamorphism, respectively (see Somin *et al.*, 1992; Millán, 1996). Lázaro & García-Casco (2008) provided evidence for high-temperature fluid-rock processes that generated, at near-peak conditions, trondhjemites by partial melting and hornblendites by metasomatic alteration of amphibolites. Our observations indicate that banded zoisite-rich rocks are metasomatic products formed at high temperature. Consequently, in the light of our data and interpretations, the 105–103 Ma ages should be reinterpreted as a reflection of fluid-rock processes at near-peak metamorphic temperature, during the near-isobaric cooling stage in the upper plate prior to formation of the subduction channel. On the other hand, taking into account our calculated onset of subduction at *c.* 120 Ma (Figs 12 & 13), the 126–120 Ma age interpreted by Hatten *et al.* (1989) as formation of the oceanic protolith of the zoisitite would indicate a very young subducting oceanic crust (*c.* 5 Ma).

Tectonic implications

Our data suggest that the oceanic magmatic mafic precursors of the amphibolites began to be subducted at *c.* 120 Ma (Figs 12 & 13). These rocks followed a counterclockwise *P–T* path, consistent with an onset of subduction scenario (Perchuk *et al.*, 1999; Gerya *et al.*, 2002; Wakabayashi, 2004; Willner *et al.*, 2004; Vignaroli *et al.*, 2005; Krebs *et al.*, 2008). Thus, the rocks studied here document the early history of subduction in the region, which probably began at *c.* 120 Ma. This is in agreement with regional geological arguments (Pindell & Dewey, 1982; Pindell, 1993; Pindell & Kennan, 2001; Pindell *et al.*, 2005, 2006), suggesting the onset of subduction of the Protocaribbean (Atlantic) lithosphere during the Aptian (*c.* 120 Ma), and with independent estimates by Krebs *et al.* (2008) from the Rio San Juan complex (Dominican Republic).

The amphibolites of the Sierra del Convento were metamorphosed to relatively high temperature (700–750 °C) and moderate pressure (~15 kbar), and underwent partial melting processes which formed trondhjemitic liquids (García-Casco *et al.*, 2008a). The relatively shallow (~50 km) conditions of melting of oceanic crust in the Sierra del Convento point to an abnormally high geothermal environment during subduction. The age of the subducting slab critically influences the geothermal gradient in the subduction environment (Gerya *et al.*, 2002), causing the slab–mantle interface to reach melting conditions at shallow depths upon subduction of young lithosphere (e.g. Okudaira & Yoshitake, 2004; Uehara & Aoya, 2005). Pindell *et al.* (2005, 2006) have indicated that the onset of subduction during the Aptian consumed young oceanic lithosphere of the Protocaribbean basin, which was opening at that time, and Krebs *et al.* (2008) provided geochronological evidence for *c.* 20 Ma as the age of the initially subducted lithosphere during the Aptian. The fact that the metamorphic gradient for the initially subducted lithosphere is higher in the Sierra del Convento than in the Río San Juan mélange is consistent with a younger age of the subducting lithosphere in the former, and implies that the Protocaribbean ridge was closer to eastern Cuba by the Aptian (García-Casco *et al.*, 2008a). This is in agreement with the *c.* 5 Ma age for subducting curst inferred from the 126–120 Ma age of the subducted protolith in the Sierra del Convento (Hatten *et al.*, 1989). Thus, the rocks from the Sierra del Convento mélange represent a direct evidence for Aptian onset of subduction of very young Protocaribbean lithosphere in the Caribbean region.

CONCLUSIONS

SHRIMP U-Pb (zircon) and Ar/Ar (amphibole) data from exotic blocks of amphibolite and associated trondhjemite–tonalite (formed after partial melting of the amphibolites) from the Sierra del Convento mélange provide a crystallization age of *c.* 113 Ma and two groups of cooling ages of 106–97 Ma (cooling of metamorphic/magmatic pargasite) and 87–83 Ma (growth/cooling of retrograde overprints). The mélange blocks followed counterclockwise *P–T* paths consisting of several stages, including: (i) hot subduction (only amphibolites) during 120–115 Ma; (ii) relatively fast near-isobaric cooling in the upper plate at 15 kbar from peak metamorphic/magmatic conditions at ~750 °C to 550 °C during 115–107 Ma; (iii) slow syn-subduction cooling and exhumation in the subduction channel during 107–70 Ma, and (iv) fast syn-collision cooling and exhumation during 70–60 Ma. The model *P–T–t* of the studied rocks indicates that the onset of subduction in the region was at *c.* 120 Ma, in agreement with independent estimates. The average cooling and exhumation rates within the subduction channel during the syn-subduction stage were ~4 °C Myr^{-1} and 0.7 km Myr^{-1}, respectively, comparable with rates determined elsewhere in intra-oceanic subduction environments. Subsequently, collision in the region triggered much

faster rates of cooling and exhumation of ~80 °C Myr^{-1} and 5 km Myr^{-1}.

ACKNOWLEDGEMENTS

We thank K. Núñez-Cambra and A. Rodríguez-Vega for field assistance, the ARGONAUT laboratory team (Salzburg, Austria) for technical assistance during Ar-dating, and M. Wingate for help during SHRIMP analyses in Perth, Australia. Y. Rojas-Agramonte acknowledges a Humboldt Foundation Georg Forster fellowship and a postdoctoral fellowship of the Geocycles cluster of Mainz University. This is a contribution to IGCP-546 'Subduction zones of the Caribbean' and is Mainz Geocycles contribution No. 387. We also appreciate financial support from the Spanish MEC project CGL2006-08527/BTE.

REFERENCES

Adamovich, A. & Chejovich, V., 1964. Principales características de la geología y de los minerales útiles de la región nordeste de la Provincia de Oriente. *Revista Tecnológica*, **2,** 14–20.

Anczkiewicz, R., Platt, J. P., Thirlwall, M. F. & Wakabayashi, J., 2004. Franciscan subduction off to a slow start: evidence from high-precision Lu–Hf garnet ages on high grade-blocks. *Earth and Planetary Science Letters*, **225,** 147–161.

Baldwin, S. L., Harrison, T. M. & Fitz Gerald, J. D., 1990. Diffusion of ^{40}Ar in metamorphic hornblende. *Contributions to Mineralogy and Petrology*, **105,** 691–703.

Baldwin, S. L., Monteleone, B. D., Webb, L. E. *et al*., 2004. Pliocene eclogite exhumation at plate tectonic rates in eastern Papua New Guinea. *Nature*, **431,** 263–267.

Black, L. P., Kamo, S. L., Allen, C. M. *et al*., 2003. TEMORA 1: a quality zircon standard for Phanerozoic U-Pb geochronology. *Chemical Geology*, **200,** 155–170.

Boiteau, A., Saliot, P. & Michard, A., 1972. High-pressure metamorphism in Ophiolite Complex of Purial (Oriente, Cuba). *Comptes Rendus Hebdomadaires Des Seances De L Academie Des Sciences Serie D*, **274,** 2137–2140.

Cloos, M., 1982. Flow melanges: numerical modelling and geologic constraints on their origin in the Franciscan subduction complex, California. *Geological Society of America Bulletin*, **93,** 330–345.

Cobiella, J., Quintas, F., Campos, M. & Hernández, M., 1984. *Geología de la Región Central y Suroriental de la Provincia de Guantánamo*. Editorial Oriente, Santiago de Cuba, Santiago de Cuba, 125 p.

Compston, W., Williams, I. S., Kirschvink, J. L. *et al*., 1992. Zircon U-Pb ages for the Early Cambrian time scale. *Journal Geological Society London*, **149,** 171–184.

Dahl, P. S., 1996. The effects of composition on retentivity of argon and oxygen in hornblende and related amphiboles: a field-tested empirical model. *Geochimica et Cosmochimica Acta*, **60,** 3687–3700.

De Laeter, J. R. & Kennedy, A. K., 1998. A double focusing mass spectrometer for geochronology. *International Journal of Mass Spectrometry*, **178,** 43–50.

Duchêne, S., Blichert-Toft, J., Luais, B. *et al*., 1997. The Lu-Hf dating of garnets and the ages of the Alpine high-pressure metamorphism. *Nature*, **387,** 586–589.

Ernst, W. G., 1988. Tectonic history of subduction blueschists *P-T* paths. *Geology*, **16,** 1081–1084.

García-Casco, A., 2007. Magmatic paragonite in trondhjemites from Sierra del Convento mélange, Cuba. *American Mineralogist*, **92,** 1232–1237.

García-Casco, A., Torres-Roldán, R. L., Millán, G. *et al*., 2001. High-grade metamorphism and hydrous melting of metapelites in the Pinos terrane (W. Cuba): evidence for crustal thickening and extension in the northern Caribbean collisional belt. *Journal of Metamorphic Geology*, **19,** 699–715.

García-Casco, A., Torres-Roldán, R. L., Iturralde-Vinent, M. A. *et al*., 2006. High pressure metamorphism of ophiolites in Cuba. *Geologica Acta*, **4,** 63–88.

García-Casco, A., Lázaro, C., Rojas Agramonte, Y. *et al*., 2008a. Partial melting and counterclockwise *P-T* path of subducted oceanic crust (Sierra del Convento mélange, Cuba). *Journal of Petrology*, **49,** 128–161.

García-Casco, A., Iturralde-Vinent, M. A. & Pindell, J., 2008b. Latest Cretaceous collision/accretion between the Caribbean Plate and Caribeana: origin of metamorphic terranes in the Greater Antilles. *International Geology Review*, **50,** 781–809.

Gerya, T. V., Stoeckhert, B. & Perchuk, A. L., 2002. Exhumation of high-pressure metamorphic rocks in a subduction channel – a numerical simulation. *Tectonics*, **21,** 6–1 – 6–19.

Gradstein, F. M. & Ogg, J. G., 2005. *Time Scale Encyclopedia of Geology. 5*. United Kingdom Elsevier Academic Press, Oxford.

Handler, R., Neubauer, F., Velichkova, S. H. & Ivanov, Z., 2004. $^{40}Ar/^{39}Ar$ age constraints on the timing of magmatism and post-magmatic cooling in the Panagyurishte region, Bulgaria. *Schweizerische Mineralogische und Petrographische Mitteilungen*, **84,** 119–132.

Harrison, T. M., 1981. Diffusion of ^{40}Ar in hornblende. *Contributions to Mineralogy and Petrology*, **78,** 324–331.

Hatten, C. W., Mattison, J. M., Renne, P. R. *et al*., 1989. Rocas metamórficas de alta presión: nuevos datos acerca de sus edades. Primer Congreso Cubano de Geología, La Habana (Cuba), pp. 118–119.

Hernández, M. & Canedo, Z., 1995. Geoquímica de las ofiolitas meridionales de Cuba oriental. In: *Revista de Minería y Geología*, pp. 3–9, University of Moa, Moa, Cuba.

Holland, T. J. B. & Powell, R., 1998. An internally consistent thermodynamic data set for phases of petrological interest. *Journal of Metamorphic Geology*, **16,** 309–343.

Iturralde-Vinent, M., 1976. Estratigrafía de la zona Calabazas-Achotal, Mayarí Arriba, Oriente. In: *Revista La Minería en Cuba. 5*, pp. 9–23.

Iturralde-Vinent, M., 1977. Estratigrafía de la zona Calabazas-Achotal, Mayarí Arriba, Oriente. In: *Revista La Minería en Cuba, 6*, pp. 32–44.

Iturralde-Vinent, M. A., 1998. Sinopsis de la Constitución Geológica de Cuba. *Acta Geológica Hispánica*, **33,** 9–56.

Iturralde-Vinent, M. A., Millán, G., Korkas, L. *et al*., 1996. Geological interpretation of the Cuban K-Ar data base. In: *Ofiolitas Y Arcos Volcánicos de Cuba* (ed. Iturralde-Vinent, M. A.), pp. 48–69, IGCP Project 364, Miami, FL.

Iturralde-Vinent, M. A., Díaz Otero, C., Rodríguez Vega, A. & Díaz Martínez, R., 2006. Tectonic implications of paleontologic dating of Cretaceous-Danian sections of Eastern Cuba. *Geologica Acta*, **4,** 89–102.

Kinny, P. D., 1986. 3820 Ma zircons from a tonalitic Amitsoq gneiss in the Godthab district of southern West Greenland. *Earth and Planetary Science Letters*, **79,** 337–347.

Krebs, M., Maresch, W. V., Schertl, H.-P. *et al*., 2008. E. The dynamics of intra-oceanic subduction zones: a direct comparison between fossil petrological evidence (Rio San Juan Complex, Dominican Republican) and numerical simulation. *Lithos*, **103,** 106–137.

Kretz, R., 1983. Symbols for rock-forming minerals. *American Mineralogist*, **68,** 277–279.

Kulachkov, L. V. & Leyva, R. C., 1990. *Informe sobre los resultados de los trabajos de reconocimiento geológico para cuarzo filoniano en la parte oriental de Cuba*. Instituto Superior Minero-Metalúrgico, Moa, Cuba.

Lázaro, C. & García-Casco, A., 2008. Geochemical and Sr-Nd isotope signatures of pristine slab melts and their residues (Sierra del Convento mélange, eastern Cuba). *Chemical Geology*, **255,** 120–133.

Leake, B. E., Woolley, A. R., Arps, C. E. S. *et al*., 1997. Nomenclature of amphiboles: Report of the Subcommittee on Amphiboles of the International Mineralogical Association, Commission on New Minerals and Mineral Names. *American Mineralogist*, **82,** 1019–1037.

Leyva, R. C., 1996. Características geológicas, regularidades de distribución y perspectivas de utilización del cuarzo filoniano de la región oriental de Cuba. Master′s Thesis, University of Moa, Moa, Cuba.

Ludwig, K. R., 2001. *Isoplot/*Ex – A Geochronological Toolkit for Microsoft Excel. Special Publication No 1a, Berkeley Geochronological Center, 2455 Ridge Road.

Marchesi, C., Garrido, C. J., Godard, M. *et al*., 2006. Petrogenesis of highly depleted peridotites and gabbroic rocks from the Mayarí-Baracoa Ophiolitic Belt (eastern Cuba). *Contributions to Mineralogy and Petrology*, **151,** 717–736.

McDougall, I. & Harrison, T. M., 1999. *Geochronology and Thermochronology by the* $^{40}Ar/^{39}Ar$ Method. Oxford University Press, Oxford.

Millán, G., 1996. Metamorfitas de la asociación ofiolítica de Cuba. In: *Ofiolitas y Arcos Volcanicos de Cuba* (ed. Iturralde-Vinent, M. A.), pp. 147–153, IGCP Project 364, Miami, FL.

Monié, P., Torres-Roldán, R. L. & García-Casco, A., 1994. Cooling and exhumation of the Western Betic Cordilleras, $^{40}Ar/^{39}Ar$ thermochronological constraints on a collapsed terrane. *Tectonophysics*, **238,** 353–379.

Nelson, D. R., 1997. Compilation of SHRIMP U-Pb zircon geochronology data, 1996. Geological Survey Western Australia, Record 1997/2, p. 189.

Okudaira, T. & Yoshitake, Y., 2004. Thermal consequences of the formation of a slab window beneath the Mid-Cretaceous southwest Japan arc: a 2-D numerical analysis. *The Island Arc*, **13,** 520–532.

Perchuk, A. L., Philippot, P., Erdmer, P. & Fialin, M., 1999. Rates of thermal equilibration at the onset of subduction deduced from diffusion modeling of eclogitic garnets, Yukon-Tanana terrain. *Geology*, **27,** 531–534.

Pindell, J. L., 1993. Regional synopsis of Gulf of Mexico and Caribbean evolution. In: *Mesozoic and Early Cenozoic Development of the Gulf of Mexico and Caribbean Region – A Context for Hydrocarbon Exploration* (eds Pindell, J. L. & Perkins, R. F.) Selected Papers Presented at the GCSSEPM Foundation 13th Annual Research Conference, Gulf Coast Section SEPM, Houston, Texas, 251–274.

Pindell, J. L. & Dewey, J. F., 1982. Permo-Triassic reconstruction of western Pangea and the evolution of the Gulf of Mexico/ Caribbean region. *Tectonics*, **1,** 179–211.

Pindell, J. L. & Kennan, L., 2001. *Kinematic Evolution of the Gulf of Mexico and Caribbean. Transactions, Petroleum Systems of Deep-water Basins: Global and Gulf of Mexico Experience*. GCSSEPM 21st Annual Research Conference, Houston, TX, USA, 193–220.

Pindell, J. L., Kennan, L., Maresch, W. V. *et al*., 2005. Plate-kinematics and crustal dynamics of circum-Caribbean arc-continent interactions: Tectonic controls on basin development in Proto-Caribbean margins. In: *Caribbean-South American plate interactions, Venezuela* (eds Avé Lallemant, H. G. & Sisson, V. B.), Special Paper 394-Geological Society of America. Geological Society of America, Boulder, CO. pp. 7–52.

Pindell, J. L., Kennan, L., Stanek, K. P., Maresch, W. V. & Draper, G., 2006. Foundations of Gulf of Mexico and Caribbean evolution: eight controversies resolved. *Geologica Acta*, **4,** 303–341.

Powell, R. & Holland, T. J. B., 1994. Optimal geothermometry and geobarometry. *American Mineralogist*, **79,** 120–133.

Proenza, J. A., Díaz-Martínez, R., Iriondo, A. *et al*., 2006. Primitive Cretaceous island-arc volcanic rocks in eastern Cuba: the Téneme Formation. *Geologica Acta*, **4,** 103–121.

Reiners, P. W., Ehlers, T. A., Garver, J. I. *et al*., 2002. Late Miocene exhumation and uplift of the Washington Cascade Range. *Geology*, **30,** 767–770.

Ring, U. & Reischmann, T., 2002. The weak and superfast Cretan detachment, Greece: exhumation at subduction rates in extruding wedges. *Journal of the Geological Society of London*, **159,** 225–228.

Rubatto, D. & Hermann, J., 2001. Exhumation as fast as subduction? *Geology*, **29,** 3–6.

Somin, M. & Millán, G., 1981. *Geology of the Metamorphic Complexes of Cuba (in Russian)*. Nauka, Moscow.

Somin, M. L., Arakelyants, M. M. & Kolesnikov, E. M., 1992. Age and tectonic significance of high-pressure metamorphic rocks in Cuba. *International Geology Review*, **34,** 105–118.

Stanek, K. P., Maresch, W. V., Grafe, F. *et al*., 2006. Structure, tectonics and metamorphic development of the Sancti Spiritus Dome (eastern Escambray massif, Central Cuba). *Geologica Acta*, **4,** 151–170.

Steiger, R. H. & Jäger, E., 1977. Subcommission on geochronology: Convention on the use of decay constants in geo-and cosmochronology. *Earth and Planetary Science Letters*, **36,** 359–362.

Stern, R. A., 1997. The GSC sensitive high resolution ion microprobe (SHRIMP): Analytical techniques of zircon U-Th-Pb age determinations and performance evaluation. In: *Radiogenic Age and Isotope Studies*, report 10. Geological Survey of Canada, Current Research 1997-F, pp. 1–31.

Tsujimori, T., Matsumoto, K., Wakabayashi, J. & Liou, J. G., 2006. Franciscan eclogite revisited: Reevaluation of the P–T evolution of tectonic blocks from Tiburon Peninsula, California, U.S.A. *Mineralogy and Petrology*, **88,** 243–267.

Uehara, S. & Aoya, M., 2005. Thermal model for approach of a spreading ridge to subduction zones and its implications for high P/high T metamorphism: Importance of subduction vs ridge-approach ratio. *Tectonics*, **24,** TC4007. doi: 10.1029/2004TC001715.

Vielzeuf, D. & Schmidt, M. W., 2001. Melting reactions in hydrous systems revisited: applications to metapelites, metagreywackes and metabasalts. *Contributions to Mineralogy and Petrology*, **141,** 251–267.

Vignaroli, G., Rossetti, F., Bouybaouene, M. *et al*., 2005. A counter-clockwise *P-T* path for the Voltri Massif eclogites (Ligurian Alps, Italy). *Journal of Metamorphic Geology*, **23,** 533–555.

Wakabayashi, J., 2004. Tectonic mechanisms associated with P–T paths of regional metamorphism: Alternatives to single-cycle thrusting and heating. *Tectonophysics*, **392,** 193–218.

Wallis, S., Moriyama, Y. & Tagami, T., 2004. Exhumation rates and age of metamorphism in the Sanbagawa belt: new constraints from zircon fission track analysis. *Journal of Metamorphic Geology*, **22,** 17–24.

Wijbrans, J. R., Pringle, M. S., Koppers, A. A. P. & Scheveers, R., 1995. Argon geochronology of small samples using the Vulkaan argon laserprobe. *Proceedings of the Koninklijke Nederlandse Akademie Van Wetenschappen*, **98,** 185–218.

Williams, I. S., 1998. U-Th-Pb geochronology by ion microprobe. In: *Applications of Microanalytical Techniques to Understanding Mineralizing Processes* (eds McKibben, M. A., Shanks, W. C. & Ridley, W. I.). *Reviews in Economic Geology*, **7**, 1–35.

Willner, A. P., Glodny, J., Gerya, T. V. *et al*., 2004. A counterclockwise PTt path of high-pressure/low-temperature rocks from the Coastal Cordillera accretionary complex of south-central Chile: constraints for the earliest stage of subduction mass flow. *Lithos*, **75,** 283–310.

Received 14 November 2007; revision accepted 16 October 2008.